Assimilating Sentinel-2 data in a modified vegetation photosynthesis and respiration model (VPRM) to improve the simulation of croplands CO2 fluxes in Europe

Hassan Bazzi, Philippe Ciais, Ezzeddine Abbessi, David Makowski, Diego Santaren, Eric Ceschia, Aurore Brut, Tiphaine Tallec, Nina Buchmann, Regine Maier, et al.

International Journal of Applied Earth Observation and Geoinformation 127 (2024) 103666

Contents lists available at ScienceDirect

International Journal of Applied Earth Observation and Geoinformation

journal homepage: www.elsevier.com/locate/jag

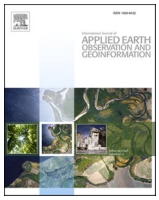

Assimilating Sentinel-2 data in a modified vegetation photosynthesis and respiration model (VPRM) to improve the simulation of croplands CO_2 fluxes in Europe

Hassan Bazzi [a,b,*], Philippe Ciais [c], Ezzeddine Abbessi [a,c], David Makowski [a], Diego Santaren [c], Eric Ceschia [d], Aurore Brut [d], Tiphaine Tallec [d], Nina Buchmann [e], Regine Maier [e], Manuel Acosta [f], Benjamin Loubet [g], Pauline Buysse [g], Joël Léonard [h], Frédéric Bornet [h], Ibrahim Fayad [c], Jinghui Lian [c], Nicolas Baghdadi [i], Ricard Segura Barrero [j], Christian Brümmer [k], Marius Schmidt [l], Bernard Heinesch [m], Matthias Mauder [n], Thomas Gruenwald [n]

[a] Université Paris-Saclay, AgroParisTech, INRAE, UMR 518 MIA Paris-Saclay, 91120 Palaiseau, France
[b] Atos France, Technical Services, 80 Quai Voltaire, 95870 Bezons, France
[c] Laboratoire des Sciences du Climat et de l'Environnement, UMR 1572 CEA-CNRS-UVSQ, Université Paris-Saclay, 91191 Gif-sur-Yvette CEDEX, France
[d] CESBIO, Université de Toulouse, CNES/CNRS/INRAE/IRD/UPS, Toulouse, France
[e] ETH Zurich, Department of Environmental Systems Science, Institute of Agricultural Sciences, Zurich, Switzerland
[f] Global Change Research Institute, Czech Academy of Sciences, the Czech Republic
[g] UMR ECOSYS, INRAE-AgroParisTech, Université Paris-Saclay, 91120 Palaiseau, France
[h] BioEcoAgro Joint Research Unit, INRAE, Université de Liège, Université de Lille, Université de Picardie Jules, Verne, 02000 Barenton-Bugny, France
[i] INRAE, UMR TETIS, University of Montpellier, AgroParisTech, 500 Rue François Breton, CEDEX 5, 34093 Montpellier, France
[j] Sostenipra Research Group (SGR 01412), Institute of Environmental Sciences and Technology (MDM-2015-0552), Z Building, Universitat Autònoma de Barcelona (UAB), Campus UAB, 08193 Bellaterra, Barcelona, Spain
[k] Thünen Institute of Climate-Smart Agriculture, 38116 Braunschweig, Germany
[l] Agrosphere Institute, IBG-3, Forschungszentrum Jülich GmbH, Germany
[m] ULiege - GxABT, TERRA Teaching and Research Center, BioDynE research axis, B-5030 Gembloux, Belgium
[n] TU Dresden, Institut für Hydrologie und Meteorologie, Professur für Meteorologie, 01062 Dresden, Germany

ARTICLE INFO

Keywords:
Carbon Cycle
Data-driven Modelling
Crop Types
Sentinel-2
MODIS
Eddy covariance

ABSTRACT

In Europe, the heterogeneous features of crop systems with majority of small to medium sized agricultural holdings, and diversity of crop rotations, require high-resolution information to estimate cropland Net Ecosystem Exchange (NEE) and its two main components of Gross Ecosystem Exchange (GEE) and the Ecosystem Respiration (R_{ECO}). In this context, this paper presents an assimilation of high-resolution Sentinel-2 indices with eddy covariance measurements at selected European cropland flux sites in a new modified version of Vegetation Photosynthesis Respiration Model (VPRM). VRPM is a data-driven model simulating CO_2 fluxes previously applied using satellite-derived vegetation indices from the Moderate Resolution Imaging Spectroradiometer (MODIS). This study proposes a modification of the VPRM by including an explicit soil moisture stress function to the GEE and changing the equation of R_{ECO}. It also compares the model results driven by S2 indices instead of MODIS. The parameters of the VPRM model are calibrated using eddy-covariance data. All possible parameters optimization scenarios include the use of the initial version vs. the proposed modified VPRM, S2, or MODIS vegetation indices, and finally the choice of calibrating a single set of parameters against observations from all crop types, a set of parameters per crop type, or one set of parameters per site. Then, we focus the analysis on the improvement of the model with distinct parameters for different crop types vs. parameters optimized without distinction of crop types. Our main findings are: (1) the superiority of S2 vegetation indices over MODIS for cropland CO_2 fluxes simulations, leading to a root mean squared error (RMSE) for NEE of less than 3.5 $\mu molm^{-2}s^{-1}$ with S2 compared to 5 $\mu molm^{-2}s^{-1}$ with MODIS (2) better performances of the modified VPRM

* Corresponding author at: Université Paris-Saclay, AgroParisTech, INRAE, UMR 518 MIA Paris-Saclay, 91120 Palaiseau, France.
E-mail address: hassan.bazzi@atos.net (H. Bazzi).

https://doi.org/10.1016/j.jag.2024.103666
Received 3 April 2023; Received in revised form 28 December 2023; Accepted 18 January 2024
Available online 29 January 2024

version leading to a significant improvement of $R_{ECO,}$ and (3) better performances when the parameters are optimized per crop-type instead of for all crop types lumped together, with lower RMSE and Akaike information criterion (AIC), despite a larger number of parameters. Associated with the availability of crop-type land cover maps, the use of S2 data and crop-type modified VPRM parameterization presented in this study, provide a step forward for upscaling cropland carbon fluxes at European scale.

1. Introduction

Studying the carbon cycle requires precise monitoring of the Net Ecosystem Exchange (NEE) of carbon dioxide (CO_2) between the terrestrial biosphere and the atmosphere (Beer et al., 2010; Reichstein et al., 2013) as well as of its two component fluxes, the Gross Ecosystem Exchange (GEE) and the Ecosystem Respiration (R_{ECO}). Croplands represent 12 % of the global vegetated areas and contribute to 16 % of global NEE (Hicke et al., 2004; Potter et al., 1993). Between 2003 and 2019, cropland area increased by 9 %, but NEE increased by 25 % (Potapov et al., 2021) due to intensification from irrigation, fertilizers, and better cultivars (Zeng et al., 2014). In the European Union, croplands cover 157 million hectares, that is 38 % of the total land area. A better monitoring of the CO_2 fluxes in cropland can help better understand the drivers of crop yields, improve resource supply (Marshall et al., 2018; Reeves et al., 2005), analyze the impacts of climate change on cropland productivity (Ciais et al., 2010, 2005; He et al., 2022), and inform policies for improving the C budget for croplands (Pique et al., 2020).

Remote sensing offers a powerful tool for land surface monitoring at large scales especially with the advances in deep learning models (Hong et al., 2023; Hong et al., 2023) . Remote sensing data combined with deep learning approaches have been applied in several geoscience applications, including and not limited to, land cover mapping (Ienco et al., 2019), forests heights and biomass estimations (Fayad et al., 2023), and most recently in CO_2 fluxes estimations (Nathaniel et al., 2023). However, given the complexity of deep learning approaches and the sparse flux measurements of the CO_2 fluxes, only few studies have explored the use of deep learning approaches in CO_2 fluxes estimations. Recently, using MODIS (Moderate Resolution Imaging Spectroradiometer) satellite data at 500 m spatial resolution, Nathaniel et al. (2023) applied a *meta*-learning procedure to train a model to learn from sparse data (sparse eddy-covariance flux measurements) to estimate CO_2 fluxes at large scales. They reported that *meta*-learning better estimated fluxes in critical regions (such as semi-arid or tropical regions) especially in extreme cases. Pabon-Moreno et al. (2022) assessed the potential of Sentinel-2 (S2) spectral bands at 10 m spatial resolution to estimate GEE using linear regression and random forest. They report that despite the good accuracy obtained for predicting the GEE using machine learning techniques, optical remote sensing information alone was not enough to predict GEE under water-stress conditions.

Specifically for cropland CO_2 fluxes, models driven by remote sensing vegetation indices, such as SAFY-CO_2 and SAFY-WB, have been extensively used to simulate NEE. These models give good performances at sites after calibration but may have limitations for large scale applications (Battude et al., 2016; Pique et al., 2020; Revill et al., 2013). Other models are more complex and calculate carbon fluxes at a half-hourly time step based on processing land surface models (Jung et al., 2020; Keenan et al., 2016; Krinner et al., 2005; Kuppel et al., 2012; Santaren et al., 2014, 2014; Sellers et al., 1986). These process-based land surface models have many parameters that are difficult to calibrate (Santaren et al., 2014). Land surface models such as the ORCHIDEE, CLM (Community Land Model), JULES (Joint UK Land Environment Simulator), and LPJ GUESS (Lund-Potsdam-Jena General Ecosystem Simulator) included parameterizations for crops, yet without detailed information on varieties and management practices (Chen et al., 2015; Di Paola et al., 2016; Lawrence and Chase, 2007; Levis et al., 2012; Smith et al., 2014, 2001).

In this study, we chose to use the data-driven Vegetation Photosynthesis Respiration Model (VPRM) (Mahadevan et al., 2008) for estimating cropland NEE and its components. One advantage of this model is that it includes a limited number of parameters that can be optimized using flux tower data. VPRM is driven by remote sensing derived vegetation indices and climatic data. It was calibrated against eddy-covariance flux measurements over the American continent (Mahadevan et al., 2008) and Europe (Kountouris et al., 2018). Generally, VPRM uses MODIS derived Enhanced Vegetation Index (EVI) and the Land Surface Water Index (LSWI) at 500 m spatial resolution in addition to temperature and radiation climatic data to describe the light dependent part (GEE) of the NEE. The ecosystem respiration flux was described by a simple function using air temperature data. The VPRM parameters were optimized using flux tower measurements grouped into nine vegetation classes including the evergreen forests, deciduous forest, mixed forest, shrublands, savannas, grassland, wetlands, and croplands. Following its validation on the USA, the VPRM was recalibrated on the European continent using 46 European eddy-covariance towers (Kountouris et al., 2018) and is currently used by the European Integrated Carbon Observation System (ICOS) to provide hourly NEE, GEE and R_{ECO} maps across the European continent between −15.0° to 35.0° east and 33.0° to 73.0° north (Gerbig and Koch, 2021).

When first developed over the USA, VPRM considered croplands as a single vegetation class regardless of the specific crop type and the inter-crop variation effects on NEE, GEE and R_{ECO}. The use of a single class of cropland might be justified in the USA by the relatively low diversity of the crop types, with maize and soybean being the two dominant cultivated annual crops. In addition, the large size of agricultural fields (exceeding 500 m in length and width) in the USA made MODIS data a reasonable choice to extract vegetation indices over the same crop cover class with no mixture of reflectance from different land covers. However, in Europe, the heterogeneous features of agricultural landscapes and the complex cropping systems with small to medium size fields, variable crop rotations, different management practices, and a diversity of crop types make the quantification of cropland NEE challenging under the assumption of a single crop type. Given the complex European agricultural context, accurate estimation of the cropland CO_2 fluxes requires detailed crop-type parametrization instead of a generic crop parametrization. However, a parametrization of VPRM per crop type expects fine spatial resolution satellite data capturing the details of crop development and photosynthetic activity with minimal interference of other land cover types. Here we opted for the S2 optical sensor from the Copernicus program which provides vegetation indices at a fine spatial resolution (between 10 and 60 m) with multispectral resolution (13 bands) and a temporal resolution reaching 5 days in Europe. To the best of our knowledge, the aspect of performing a crop-specific parametrization of the VPRM has not yet been explored.

Another limitation of the VPRM described by Mahadevan et al., (2008) was the inability of remotely sensed Land Surface Water Index (LSWI) to detect the water stress conditions and its effect on the plant photosynthesis and therefore the GEE and the R_{ECO} fluxes. They reported that the lack of a soil moisture function in the VPRM equations represented the principal source of unaccounted variance in the fluxes' simulations. Therefore, we proposed to include an additional soil moisture function for both GEE and R_{ECO} equations with the aim to better capture the effect of water stress on the photosynthetic activity.

In this study, we present a crop-specific optimization of the VPRM parameters to simulate NEE, GEE and R_{ECO} at eddy covariance mea-

surement sites from ten flux towers across Europe covering 11 different crop types between 2018 and 2020. Several scenarios for parameters optimizations were evaluated and compared including the use of MODIS or S2 vegetation indices, a generic set of parameters for all crop types vs. a different set of parameters per crop type and a set of parameters per individual site. In addition, two versions of VPRM were tested, the standard version developed by Mahadevan et al. (2008), and a modified version, proposed in this study, with an additional soil moisture stress function of GEE and a new equation for R_{ECO}. The objectives of this study are the following:

1- Compare the performances of the standard and the new VPRM versions using MODIS and S2 vegetation indices for simulating CO_2 fluxes over croplands sites in Europe.
2- Compare the performances using a default generic parameterization for all crop types vs. crop-specific parameterization of the VPRM.
3- Propose new crop specific VPRM parameterization for simulations of the CO_2 fluxes for different crop types.

2. Materials and methods

2.1. Vegetation photosynthesis and respiration model (VPRM)

The model first described by Mahadevan et al. (2008) estimates the surface fluxes (NEE, GEE and R_{ECO}) at hourly time steps from remote sensing observations and meteorological data. NEE is divided into light-dependent photosynthesis (GEE) and light-independent ecosystem respiration (R_{ECO}). Since several studies have demonstrated a close correlation between satellite-based vegetation indices such as the Enhanced Vegetation Index (EVI) and photosynthesis (Xiao, 2004; Xiao et al., 2004), GEE in VPRM is represented as:

$$GEE = \boldsymbol{\lambda} \times T_{scale} \times P_{scale} \times W_{scale} \times EVI \times \left(\frac{1}{1 + \frac{PAR}{\boldsymbol{PAR}_0}} \right) \times PAR \quad (1)$$

EVI is calculated using the near infrared, the red, and the blue bands of multispectral satellite reflectance observations (see equation A.1 in Appendix A). λ is the light use efficiency, PAR is the Photosynthetically Active Radiation, and PAR_0 the half saturation value. Since PAR values are not generally available in meteorological data as continuous spatial maps, the PAR is replaced by the shortwave radiation (SWRad) considering the close correlation between SWRad and PAR.

P_{scale} and W_{scale} are factors that account for the leaf age and water stress effects on GEE respectively and are derived from the satellite-based Land Surface Water Index (LSWI). The LSWI is calculated using the infrared and the short-wave infrared bands (see equation A.2 in Appendix A). T_{scale} represents a temperature modifier to photosynthesis. Detailed equations of $T_{scale}, P_{scale} and W_{scale}$ are presented in Appendix A (see equations A.3, A.4 and A.5 respectively).

In the standard VPRM version, R_{ECO} is modeled as a linear function of air temperature (T) given that plant and soil respiration rates increase as temperature rises as given by:

$$R_{ECO} = \boldsymbol{\alpha} \times T + \boldsymbol{\beta} \quad (2)$$

NEE represents the difference between uptake (photosynthesis) and loss (respiration) of CO_2. Following the negative sign convention that CO_2 uptake by the plant is negative, NEE is written as

$$NEE = GEE - R_{ECO} \quad (3)$$

The NEE equation proposed by Mahadevan et al. (2008) has four model parameters ($\boldsymbol{\lambda}$, $\boldsymbol{SWRad}_0$, $\boldsymbol{\alpha}$ **and** $\boldsymbol{\beta}$) that can be calibrated against flux tower data. Unit of $\boldsymbol{\lambda}$ is $\mu mol.m^{-2}s^{-1}(Wm^{-2})$), of $\boldsymbol{SWRad}_0$ is Wm^{-2}, of $\boldsymbol{\alpha}$ is $\mu molm^{-2}s^{-1}/^{\circ}C$, and of $\boldsymbol{\beta}$ is $\mu molm^{-2}s^{-1}$.

2.2. Modified vegetation photosynthesis and respiration model (MVPRM)

In this study, we propose a new version of the VPRM model with the aim to improve the model-data fitting of the fluxes NEE, GEE, and R_{ECO}. The first difference concerns the GEE equation where the effect of the soil moisture on water stress is explicitly considered. In the initial model version, this effect was accounted for implicitly through LSWI (W_{scale}). The modified version of the GEE equation includes a soil moisture function $f(\theta)$ such as:

$$GEE = \boldsymbol{f(\theta)} \times \boldsymbol{\lambda} \times T_{scale} \times P_{scale} \times W_{scale} \times EVI \times \left(\frac{1}{1 + \frac{SWRad}{\boldsymbol{SWRad}_0}} \right) \times SWRad \quad (4)$$

where $f(\theta)$ is expressed as:

$$f(\theta) = \begin{cases} q \times (\theta - \boldsymbol{\theta}^*) + 1 & \text{if } \theta \leq \boldsymbol{\theta}^* \\ 1 & \text{if } \theta > \boldsymbol{\theta}^* \end{cases} \quad (5)$$

$f(\theta)$ in the GEE is set to a value of 1 when the soil moisture value (θ) is above the critical soil moisture threshold of water stress ($\boldsymbol{\theta}^*$). Below this threshold, $f(\theta)$ is a linear function of the soil moisture deficit from $\boldsymbol{\theta}^*$, which reduces GEE under water stressed conditions. Both $\boldsymbol{q}$ and $\boldsymbol{\theta}^*$ are unitless parameters to be estimated. The soil water content is expressed in relative units (relative soil water content) and is calculated by normalizing the volumetric soil moisture to values between 0 and 1 using the minimum–maximum normalization at each flux site.

The second modification of VPRM concerns the R_{ECO} equation following Migliavacca et al. (2011) who demonstrated that climatic drivers are not sufficient to describe the temporal variability of R_{ECO} and proposed to express R_{ECO} as a function of GEE, temperature, and soil moisture as follows:

$$R_{ECO} = f(T) \times f_2(\theta) \times f(GEE) \quad (6)$$

The temperature function $f(T)$ is formulated as an exponential function of air temperature (equation (7) following the soil respiration temperature function proposed by Lloyd and Taylor (1994) with an activation energy parameter E_0 in °K, a reference temperature T_{ref} fixed at 288.15 °K (15 °C), and T_0 fixed at 227.13 °K (-46.02 °C). Air temperature is a simplification of soil and canopy temperatures and is probably justified by the fact that the air temperature is between the canopy and the soil temperature in most cases.

$$f(T) = e^{\boldsymbol{E}_0 \left(\frac{1}{T_{ref} - T_0} - \frac{1}{T - T_0} \right)} \quad (7)$$

Migliavacca et al. (2011) used precipitation as a proxy of the soil water content. However, we replaced here the precipitation function by a soil moisture function $f_2(\theta)$ since soil moisture is considered a more accurate driver of soil microbial processes affecting soil heterotrophic respiration, and plant stress affecting autotrophic respiration. Following Reichstein et al. (2002) and Reichstein (2003), the soil moisture dependency $f_2(\theta)$ of R_{ECO} is formulated as in equation (8) using the commonly applied saturation function (Bunnell et al., 1977):

$$f_2(\theta) = \frac{\theta}{\boldsymbol{\theta}_{max} + \theta} \quad (8)$$

where θ is the relative soil water content and $\boldsymbol{\theta}_{max}$ is a soil moisture threshold parameter to be optimized. θ is expressed in relative units as proposed by Reichstein (2003) and calculated by normalizing the volumetric soil water content using the minimum–maximum normalization at each flux site.

Plant (shoot and roots) respiration increases with plant biomass, thus R_{ECO} dependency to GEE is modeled with a linear relationship given by:

$$f(GEE) = \boldsymbol{R}_0 + \boldsymbol{k} \times GEE \quad (9)$$

$R_0(\mu molm^{-2}s^{-1})$ is the reference respiration which refers to the ecosystem respiration at the reference temperature (T_{ref} = 15 °C in equation (7) and under ideal soil moisture conditions (Migliavacca et al., 2011; Reichstein et al., 2002). It serves as an indicator of the site's ecosystem respiration, which is influenced by the unique site conditions, historical factors, and inherent characteristics. The parameter $\boldsymbol{k}$ (unitless) expresses the assumed response of the ecosystem respiration to GEE. R_0 and $\boldsymbol{k}$ are both parameters to be optimized.

Finally, R_{ECO} is expressed as:

$$R_{ECO} = (\boldsymbol{R}_0 + \boldsymbol{k} \times GEE) \times \left(\frac{\theta}{\boldsymbol{\theta_{max}} + \theta}\right) \times e^{E_0\left(\frac{1}{T_{ref}-T_0}-\frac{1}{T-T_0}\right)} \quad (10)$$

The new equations of GEE and R_{ECO} include a higher number of parameters. While the original version included four parameters (λ, $SWRad_0$, α and β), the new version includes eight parameters: four parameters for GEE (λ, $SWRad_0$, q and θ^*) and four parameters for R_{ECO}(R_0, k, E_0 and θ_{max}).

2.3. Dataset preparation and model-data fitting

The flowchart in Fig. 1 summarizes the dataset extraction (eddy covariance and satellite data), the VPRM and MVPRM data fitting procedure as well as the assessments performed. The use of either MODIS or S2 satellite data in the VPRM and MVRPM was tested. The VPRM and MVPRM were optimized in different scenarios considering different spatial scales using both MODIS and S2 satellite products (SN1 to SN12). The evaluation of the model-data fitting using conventional accuracy metrics was also carried out at different spatial and temporal levels. Each part of the process is explained more in details in the following subsections.

2.3.1. Eddy covariance data over croplands in Europe

Across Western and Central European countries, ten crop flux towers, part of the ICOS, were used (Fig. 2). These sites are distributed across France (4 sites), Germany (3 sites), Switzerland (1 site), Czech Republic (1 site), and Belgium (1 site). Half-hourly flux data were obtained from the FLUXNET website (https://fluxnet.org) covering a three-year period from January 2018 to December 2020 (Table A.0 in Appendix A). The standard flux data processing methodologies for correction, gap-filling, and partitioning were applied for all the sites (Pastorello et al., 2020). In addition to NEE, GEE, and R_{ECO}, the FLUXNET sheets of the 10 sites included the meteorological data (Temperature and shortwave radiation) and the volumetric soil water content (θ) at a half hourly time scale. The measured volumetric soil water content provided by the FLUXNET sheets corresponds to the topsoil layer between 0 and 20 cm depending on the sensor depth at each site.

In the standard processing of the eddy-covariance flux data, GEE and R_{ECO} are partitioned from measured NEE using either the nighttime (NT) or the daytime (DT) partitioning methods. In this study, the NT partitioning method of the R_{ECO} computed using variable Ustar (u*) (dimensionless friction velocity threshold) threshold (VUT) was used. For NEE, a variable u* threshold for each year was considered. Quality control filters were applied to eliminate unreliable half hourly observations. GEE values greater than 0 (GEE > 0), usually resulting from slight underestimation of the temperature response partitioned R_{ECO}, were set to zero and the observed NEE flux was all transferred to R_{ECO} only if u* > 0.1 and the quality flag of NEE was either measured (0) or very good gap filling (1) (Schaefer et al., 2012). Otherwise, half hourly measurements with GEE values greater than 0 were removed. Half hourly observations with zero GEE values at day-time measurements were also removed. Finally, half hourly values, where the quality flag (QC) of the NEE gap filling was poor (QC = 3), were removed. Removing a half hourly observation from one of the three CO_2 fluxes implied removing it from the three fluxes simultaneously to maintain a consistent dataset for the optimization of parameters.

In addition to the flux data, the ICOS sites investigators provided detailed information about the crop type grown each year, agricultural management, and crop calendars (Table 1). Eleven different crop types were grown across all the studied sites from 2018 to 2020. Wheat was the dominant crop type (11 cycles across all sites and years) followed by maize and rapeseed (3 cycles). Only one cycle with sugar beet and sunflower was found. Two sites (CZ-KRP and CH-OE2) included rotations with a temporary Ley for which parameters were also optimized even though it is not a conventional crop. In addition, Table 1 shows the

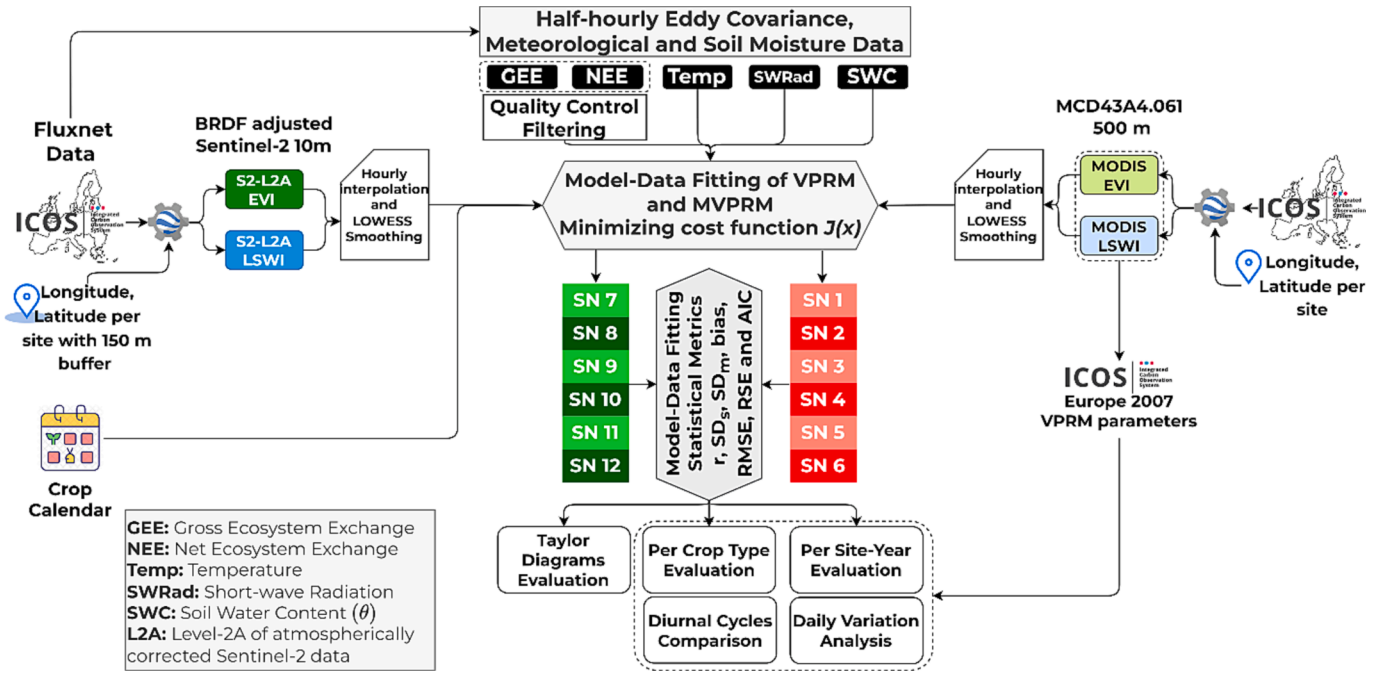

Fig. 1. Flow chart summarizing the input data preparation, the VPRM and MVPRM model-data fitting and the performed assessments.

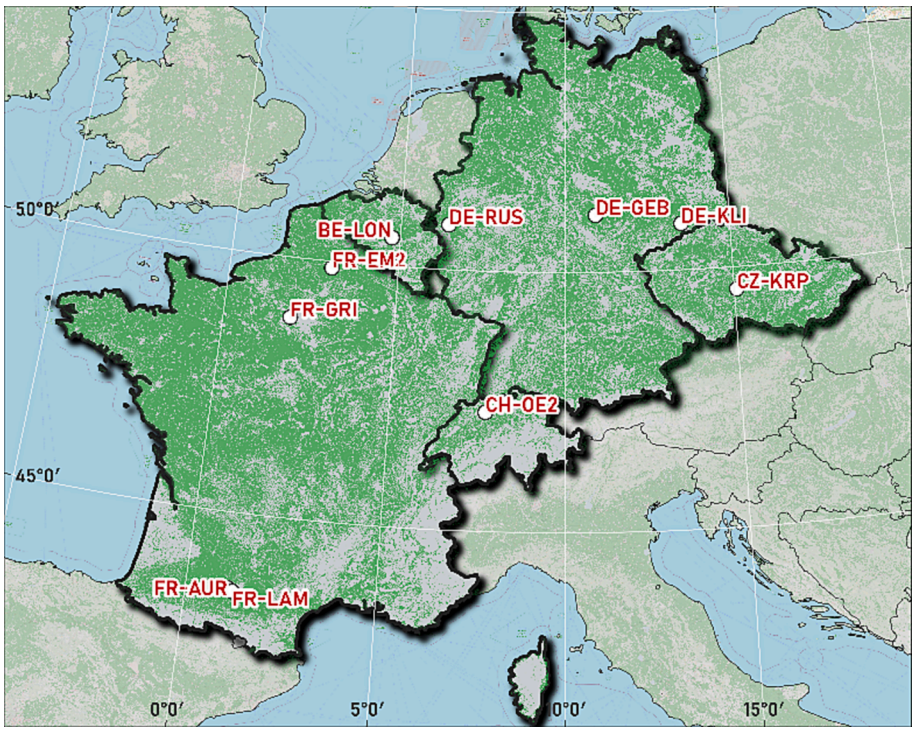

Fig. 2. Location of the studied crop flux towers. Green areas represent the cropland cover derived from Corine Land Cover Map 2018. (For interpretation of the references to color in this figure legend, the reader is referred to the web version of this article.)

Table 1
Description of the ten flux tower sites with their corresponding crop calendar between 2018 and 2020.

Site	Lat, Lon (°)	Elevation (m)	Slope (%)	%Cropland in 500 *m*	Crop 2018	Crop 2019	Crop 2020
FR-LAM	43.4964°, 1.2378°	181 *m*	Flat	67.6 %	Wheat	Maize	Wheat
FR-AUR	43.5496°, 1.1061°	250 *m*	(5 – 10 %)	82.6 %	Rapeseed	Wheat	Sunflower
FR-GRI	48.8442°, 1.9519°	125 *m*	< 2 %	90.3 %	Wheat	Maize	Wheat
FR-EM2	49.8721°, 3.0206°	85 *m*	Flat	100 %	Wheat/Oat	Barley/Oat	Maize
BE-LON	50.5516°, 4.74623°	170 *m*	< 2 %	96.1 %	Potato	Wheat/Bean	Sugar beet
DE-RUS	50.8659°, 6.4471°	103 *m*	Flat	100 %	Wheat	Potato	Wheat
DE-GEB	51.0997°, 10.91463°	161 *m*	Flat	100 %	Wheat	Wheat	Potato
DE-KLI	50.8930°, 13.5224°	478 *m*	Flat	87.3 %	Maize	Bean	Rapeseed
CZ-KRP	49.5732°, 15.0787°	535 *m*	(5 – 10 %)	69.5 %	Ley	Grass	Wheat
CH-OE2	47.2864°, 7.7337°	452 *m*	Flat	89.4 %	Rapeseed	Barley	Ley

percentage of cropland areas within 500 m zone (corresponding to one MODIS pixel) around each flux site extracted using the Sentinel-2 dynamic land cover map (Brown et al., 2022) (Table A.0 in Appendix A). The cropland percentage within 500 m around the eddy covariance sites ranges between 67.6 % (FR-LAM) and 100 % (pure cropland) for different sites.

2.3.2. Satellite vegetation indices

The two vegetation indices used by both VPRM versions are the EVI and the LSWI. A time series of S2 EVI and LSWI (see equations in Appendix A) were calculated for each site using all available cloud free S2 images at Level-2A atmospheric correction between 2018 and 2020 (Table A.0 in Appendix A). Bi-Directional reflectance correction (BRDF) was applied to the S2 surface reflectance bands following the BRDF adjustment of S2 multispectral images proposed by Roy et al. (2017). The extraction of the S2 EVI and LSWI was performed using the Google Earth Engine (https://earthengine.google.com/). For S2 images at 10 m spatial resolution, the average pixel values of a buffer zone of 150 m around the flux tower, corresponding to the typical spatial footprint of each eddy covariance site, was considered to calculate the corresponding EVI and LSWI at each S2 image. The 150 m buffer distance also guarantees the spatial crop-type purity of the averaged pixels within the buffer zone. MODIS EVI and LSWI at 500 m spatial resolution were also extracted for each site using the MCD43A4 product available on Google Earth Engine (Table A.0 in Appendix A). The MCD43A4 MODIS provides daily Nadir Bidirectional Reflectance Distribution Function Adjusted Reflectance (NBAR) at 500 m spatial resolution. Both S2 and MODIS indices were linearly interpolated at daily scales to obtain complete yearly time series, and then smoothed using the locally weighted least square algorithm (LOWESS) to reduce atmospheric noise in satellite data. For half-hourly scale optimization, the vegetation indices were also interpolated at half-hourly scale to match the eddy covariance measurements.

2.3.3. Optimization scenarios

In this study, the parameters were optimized for the VPRM or MVPRM versions using MODIS or S2 vegetation indices. We considered optimizing parameters for all the sites-years grouped together, for sites-years grouped per crop type (e.g., all wheat, all maize), and for each site-year (site-year notation corresponds to data at one site for one year and for each crop cycle in this year in case of more than one cycle in the year). For naming simplicity, the standard Initial and Modified VPRM are represented as (IV) and (MV) respectively. Optimization for each site-year is denoted by “Site”, grouping data per crop type is denoted by

"CropT", and grouping all sites and all years is represented by "ALL". The combination of these options produced twelve different optimization scenarios (2 models x 2 sensors x 3 grouping of observations) summarized in Table 2. The number of optimized parameters in each scenario differed according to the used VPRM version (IV or MV) and the number of independent groups considered in the scenario (number of crop types or number of sites-years).

2.3.4. Bayesian optimization

Parameters were optimized using a Bayesian inversion framework taking into consideration observation errors and prior parameter uncertainties. This framework was implemented in previous CO_2 flux estimations, using flux tower data, since it accounts for the uncertainty in the eddy covariance measurements in the optimization (Kuppel et al., 2012; Lasslop et al., 2010; Santaren et al., 2007). It assumes a Gaussian distribution for the observation errors and the parameter uncertainties (Tarantola, 1987). The set of optimized parameters corresponds thus to a minimum of a cost function denoted by $\boldsymbol{J}(\boldsymbol{x})$ and expressed as:

$$J(x) = \frac{1}{2}\left[(y_{meas} - H(x))^t \mathbf{R}^{-1}(y_{meas} - H(x)) + (x - x_b)^t \mathbf{B}^{-1}(x - x_b)\right] \quad (11)$$

The first part of $J(x)$ corresponds to the mismatch between the estimated (modeled) flux H(x) and the measured (observed) flux (y_{meas}), whereas the second part of the cost function represents the mismatch between the optimized parameters (x) and the prior mean values of the parameters (x_b). **R** is a diagonal matrix including the variances of the observations, in which we assume that the observation errors are independent. Similarly, **B** is a diagonal matrix describing the prior variances of the parameters, assuming that they are also independent. Considering that **R** and **B** are two diagonal matrices, the cost function can be expressed as a weighted least square function expressed as:

$$J(x) = \frac{1}{2}\left(\sum_{i=1}^{n} \frac{(y_{meas,i} - y_{mod,i(x)})^2}{{\sigma_{meas,i}}^2} + \sum_{j=1}^{P} \frac{(x_j - xb_j)^2}{{\sigma_{xb,j}}^2}\right) \quad (12)$$

where y_{meas} is the observed value, y_{mod} is the modeled value dependent on the parameters (x), $\sigma_{meas,i}$ is the observation uncertainty (observation error), and σ_{xb} is the error standard deviation of the prior parameter values (x_b). n and p are the numbers of observations and the number of parameters respectively.

Since NEE is the difference of GEE and R_{ECO}, we choose to optimize only NEE and GEE assuming that we have only two degrees of freedom, and that the sum relation would directly optimize the third flux (here R_{ECO}). To apply the weighted least square cost function, the half hourly observations variances on NEE and GEE were calculated. For NEE, the FLUXNET data provide an observation uncertainty value computed as the quadratic mean from the combination of the uncertainty from multiple u* thresholds and the random observation uncertainty calculated by the method proposed by Hollinger and Richardson (2005). Since the FLUXNET sheet does not provide any information about the total GEE uncertainty, the uncertainty of GEE is assumed to include the uncertainty of the gap filling algorithm, the partitioning uncertainty, the random measurement uncertainty of NEE, as well as the threshold friction velocity (u*) uncertainty (Schaefer et al., 2012). The random uncertainty of GEE was estimated using the same method for that of NEE, following Hollinger and Richardson (2005), given as the standard deviation of the measured fluxes in a sliding window of ± 7 days and ± 1 h of the time-of-day of the current timestamp sharing the same meteorological conditions (MDS gap-filling method). The GEE gap filling uncertainty was considered as a relative error (8 %) derived from the standard deviation of multiple gap filling algorithms reviewed by Moffat et al. (2007) and applied only to gap filled GEE values. The partitioning uncertainty was considered as a 10 % relative error of the GEE value (Desai et al., 2008). The u* threshold uncertainty was provided by the FLUXNET data and calculated for 40 different u* values. The four GEE uncertainties were summed in quadrature (Schaefer et al., 2012).

The prior values of the parameters (8 parameters for the MVPRM and 4 for the VPRM) were defined from the previous studies of Mahadevan et al. (2008) and Migliavacca et al. (2011) and expert knowledge. Nevertheless, a relative error of 40 % of prior parameters values was considered as a magnitude of the prior parameter uncertainty (matrix **B**) (Kuppel et al., 2012). This high relative uncertainty (40 %) was chosen to provide higher leverage of the observations' misfit in the cost function and lesser influence of the prior knowledge on parameter values in the optimization. $J(x)$ was minimized using a gradient-based method and the L-BFGS-B algorithm (Byrd et al., 1995). To account for the mismatch between the units of the parameter values and facilitate the convergence, each parameter was normalized for a value between 0 and 1 before optimization using the minimum–maximum normalization.

2.3.5. Model-data fitting evaluation

For each of the twelve scenarios in Table 2 the quality of model-data fit was assessed using the correlation coefficient between observations and simulations (r), the Root Mean Square Error (RMSE) of the simulations, the standard deviation of the measured (SD_m) and simulated data (SD_s), the Relative Squared Error (RSE) of the simulations, and the Akaike information criterion (AIC) (see Appendix A, equations A.6 to A.11). Since scenarios may have different numbers of optimized parameters, the AIC helps us to analyze the gain in performance between scenarios taking into consideration the different degrees of freedom (total number of optimized parameters in the scenario in Table 2).

To facilitate the comparative assessment of the twelve scenarios, the Taylor diagram (Taylor, 2001) was selected to represent the degree of correspondence for each scenario with observed data for the three fluxes (NEE, GEE and R_{ECO}). Taylor diagrams provide a summary of r, SD_m, SD_s, and finally the RMSE of the simulations. Assessment was first performed for all site-years together and then by grouping sites-years with the same crop type. The crop-type based assessment helps understand if some crop types are better fitted than others and allows the inter-scenario comparison between crop types. In addition, inter-scenarios

Table 2
Description of the optimization scenarios assessed in the study.

Scenario Number (SN)	Scenario Name	Satellite	VPRM Version	Optimization Configuration	Number of Parameters
(1)	MODIS_IV_ALL	MODIS	Initial Standard VPRM	All crops together	4
(2)	MODIS_MV_ALL	500 *m*	Modified VPRM	All crops together	8
(3)	MODIS_IV_CropT		Initial Standard VPRM	Per crop type	44
(4)	MODIS_MV_CropT		Modified VPRM	Per crop type	88
(5)	MODIS_IV_Site		Initial Standard VPRM	Per site-year	128
(6)	MODIS_MV_Site		Modified VPRM	Per site-year	256
(7)	S2_IV_ALL	S2	Initial Standard VPRM	All crops together	4
(8)	S2_MV_ALL	10 *m*	Modified VPRM	All crops together	8
(9)	S2_IV_CropT		Initial Standard VPRM	Per crop type	44
(10)	S2_MV_CropT		Modified VPRM	Per crop type	88
(11)	S2_IV_Site		Initial Standard VPRM	Per site-year	128
(12)	S2_MV_Site		Modified VPRM	Per site-year	256

assessment among each site-year was also presented. To enrich the quantitative assessment per crop-type and per site-year, we added to the 12 tested scenarios the results obtained using the previously performed optimization of the initial standard VPRM for Europe (Kountouris et al., 2018, 2015) which is currently used by ICOS to provide hourly NEE maps (Gerbig and Koch, 2021). The latter scenario was applied using MODIS data (the same used for optimization in 2007) and referred to as "EUR_2007". Finally, half monthly diurnal cycles and daily variations of selected scenarios were analyzed for some common crop types. It is worth mentioning that the optimizations performed with a separate set of parameters at each site-year could not be generalized for further large-scale extrapolation of the model, yet they were included as a reference representing the best possible optimization for each site.

3. Results

3.1. Model-data fitting over all crop species

Fig. 3 shows three Taylor Diagrams obtained for the three fluxes in the 12 different tested scenarios calculated for half hourly data for all sites-years together. An optimal model would be located in the bottom-right corner. The correlation coefficients across the 12 scenarios vary between 0.77 and 0.90 for NEE, between 0.80 and 0.92 for the GEE, and between 0.65 and 0.86 for R_{ECO}. Although all scenarios had a good correlation coefficient for the three fluxes, we noticed from the GEE and NEE Taylor diagrams (Fig. 3a and 3b) that scenarios using the MODIS vegetation indices (light and dark red) tended to have higher RMSE and lower correlation than those using the S2 vegetation indices (light and dark green). For example, the MODIS scenarios showed a RMSE for GEE ranging between 4.1 and 5.2 $\mu molm^{-2}s^{-1}$ depending on the optimization configuration (ALL, CropT, Site), whereas S2 scenarios had lower RMSE for GEE that ranged between 3.4 and 4.2 $\mu molm^{-2}s^{-1}$. A similar decrease in RMSE between MODIS and S2 scenarios is shown for NEE in Fig. 3a. In addition, for both NEE and GEE, the scenarios using S2 had standard deviation values closer to the observed standard deviation than the MODIS scenarios. The scenario with the initial standard VPRM, MODIS data, and a generic parameter optimization for all crops together (ALL) (SN 1 Fig. 3), as currently used for the ICOS CO_2 fluxes product (Gerbig

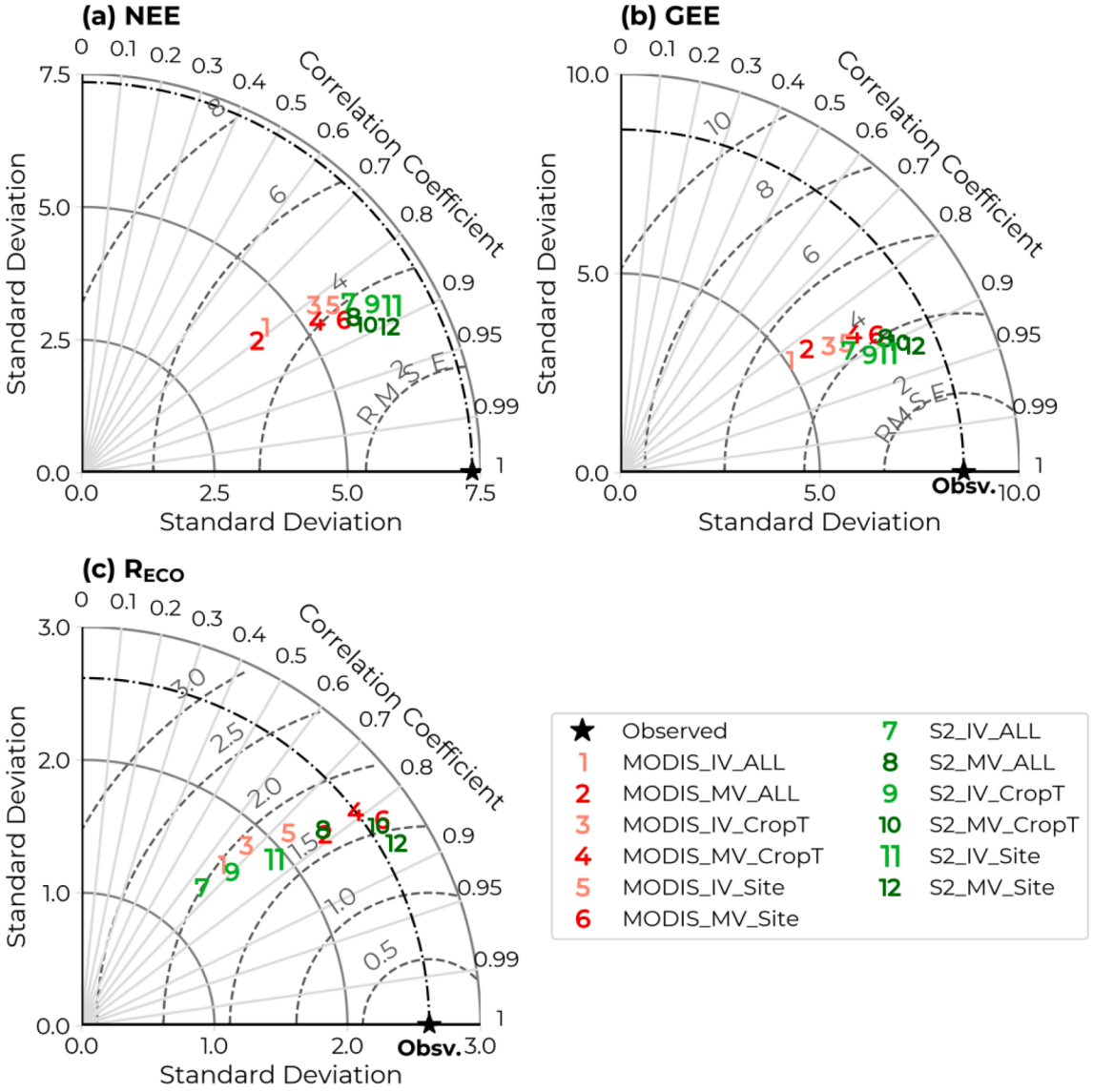

Fig. 3. Taylor Diagram for the 12 tested scenarios using half hourly data for (a) NEE, (b) GEE and (c) R_{ECO}. Green color presents S2 derived scenarios (light and dark for VPRM and MVPRM respectively). Light red and dark red colors represent MODIS derived scenarios with VPRM and MVPRM respectively. Numbers (1 to 12) represents the scenario numbers in Table 2 for different configurations. (For interpretation of the references to color in this figure legend, the reader is referred to the web version of this article.)

and Koch, 2021), failed to reproduce the observed standard deviation in both GEE and NEE for croplands. For scenario 1, the estimated SD_s of GEE reached 5 $\mu molm^{-2}s^{-1}$(4.4 $\mu molm^{-2}s^{-1}$ for NEE) compared to 8.5 $\mu molm^{-2}s^{-1}$ for observed GEE (7.3 $\mu molm^{-2}s^{-1}$ for NEE).

The comparison between scenarios from MV and IV for NEE and GEE showed a slight enhancement in both fluxes' simulations with less RMSE obtained by MV compared to the IV across scenarios using either MODIS or S2. Nevertheless, the performances of the different scenarios for R_{ECO} (Fig. 3c) clearly demonstrated that the IV (SN 1, 3, 5, 7, 9 and 11) showed a considerably less quality of model-data fit than the MV (SN 2, 4, 6, 8, 10 and 12). The RMSE of the six scenarios using IV varied between 1.7 (optimal SN 11 at site- year scale using S2) and 2 $\mu molm^{-2}s^{-1}$ (SN 1, 7 and 3). The MV had lower RMSE values for the different scenarios and reached 1.55 $\mu molm^{-2}s^{-1}$ for a S2 crop type optimization (SN 10) with an optimal RMSE at site-year optimization (Site) reaching 1.39 $\mu molm^{-2}s^{-1}$.

For both NEE and GEE, the Taylor diagrams show that the MODIS-based scenarios optimized for each crop type using IV and MV (SN 3 and 4) performed better than those optimized for all crops together and were closer to the MODIS best possible optimization at each site-year (SN 5 and 6). The modeled standard deviation became closer to the observed one and the RMSE decreased as we moved from "ALL" to "CropT. Similarly, using the S2 data, the correlation coefficient increased and the RMSE decreased as we moved from the generic scenario for all crops together (SN 7 and 8) to scenarios per crop type (SN 9 and 10). However, using S2 data, the scenarios driven by IV (SN 7, 9 and 11) had lower correlation and higher RMSE than those driven by the modified VPRM version (MV) (SN 8, 10 and 12). For both NEE and GEE, the closest scenario to the best potential optimization (SN 12) in terms of (r), SD_s and RMSE was the crop-type based scenario using S2 and MV (SN 10). This scenario showed an estimated SDs of GEE equals to 7.70 $\mu mol.m^{-2}s^{-1}$ (6.03 $\mu molm^{-2}s^{-1}$ for NEE), thus closer to observed standard deviation. The best possible optimization at site-year using the MV (SN 12) attained a GEE SD_s of 8.02 $\mu molm^{-2}s^{-1}$ (6.39 $\mu molm^{-2}s^{-1}$ for NEE). Regarding the R_{ECO}, the S2 based optimization per crop type using the MV (SN 10), with a correlation coefficient reaching 0.83, showed a better fitting of R_{ECO} than the S2 optimization for all crop types together using MV (SN 8) with a correlation of 0.77. The S2 based MV per crop type also showed a slightly better standard deviation (2.69 $\mu molm^{-2}s^{-1}$) than that of the generic optimization of all crops together (2.33 $\mu molm^{-2}s^{-1}$), and its SD_s was closer to the observed value.

In addition to the Taylor diagram, Fig. B.1 in Appendix B presents the Mean squared deviation (MSD = $RMSE^2$) for each scenario decomposed as a sum of three components: squared bias (SB), squared difference between measured and simulated standard deviation (SDSD), and lack of correlation weighted by standard deviations (LCS). A full description of the MSD decomposition is detailed in Kobayashi and Salam (2000) (see equations A.12 to A.14 in Appendix A). For NEE, the bias SB was negligible across the 12 scenarios and moderately low for the GEE where LCS was the major component of the MSD for these two fluxes. Fig. B.1 shows that the better fit of data using S2 compared to MODIS in both NEE and GEE was related to the smaller values in the lack of regression fit (LCS) indicating that S2 better simulated the pattern of the fluxes' fluctuations than MODIS. For GEE, the (MV), among all scenarios, decreased the SDSD component compared to the IV thus showing better simulation of the fluctuation magnitudes of the GEE using the MV. For the R_{ECO}, scenarios with IV represented high SB values compared to the MV whereas using the MV, both the SB and the SDSD were largely reduced which implies that the main gain in model-data fit using the MV corresponded to better fitting of both the R_{ECO} magnitudes and fluctuations.

To better appreciate the improvement of the model-data fit between scenarios, Fig. 4 shows the AIC calculated for each scenario following the AIC of weighted least squares (Akaike, 1974; Banks and Joyner, 2017). In general, lower AIC indicates a better performance. Fig. 4 shows that the AIC gradually decreased as we moved from a generic optimization for all crops (ALL) to a per crop type optimization (CropT) and finally to a per site-year optimization (Site) for both MODIS and S2, and the IV or MV model versions. From the AIC variation, we notice that scenarios with higher degrees of freedom maintained lower AIC scores. The crop-type parameterization having 88 degrees of freedom in the MV (8 MV parameters/crop-type x 11 crop types) showed lower AIC values than the generic parameterization for all crops (only 8 parameters for all crop types). This indicates that using a per crop type optimization remains significant regardless of the increase in the degrees of freedom which confirms the absence of overfitting in the optimization and guarantees that the improvement in model-data fit between a generic and a crop type parameterization is not an artifact of increasing the degrees of freedom. These results are valid for both MODIS and S2 optimization

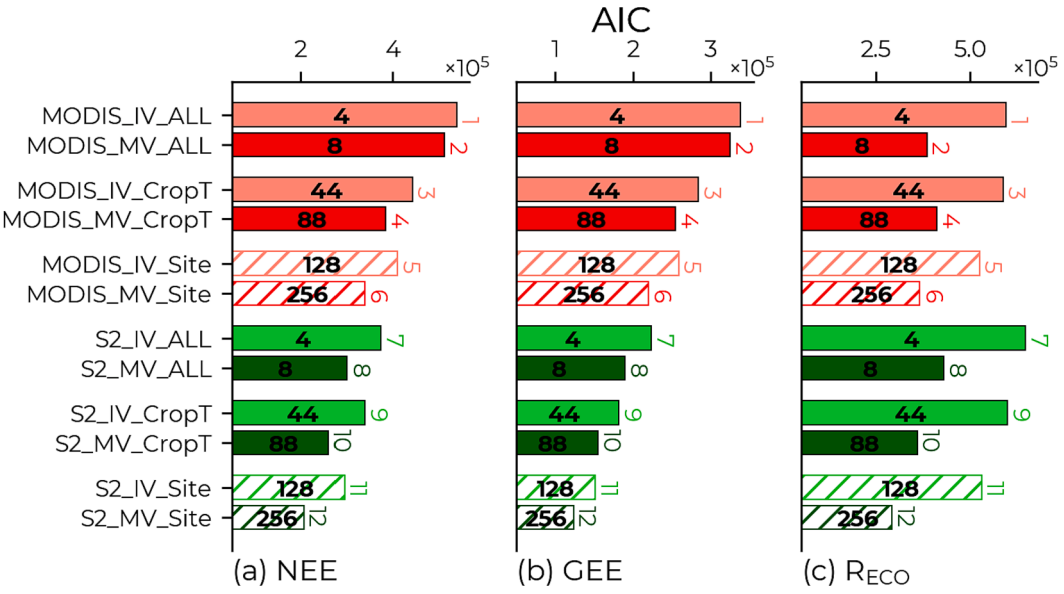

Fig. 4. AIC for the 12 scenarios calculated using half hourly data for (a) NEE, (b) GEE and (c) R_{ECO}. Hatched bars represent AIC of models where a distinct set of parameters was adjusted for each site-year. Numbers inside each bar correspond to the number of parameters optimized for each scenario while numbers above bars represent the scenario number (SN).

scenarios.

Regarding the model-data fit across different time scales, Fig. 5 presents the relative squared error (RSE) calculated at half hourly, daily averaged, and weekly scales. In addition, Appendix B presents the Taylor diagrams of daily (Fig. B.2) and weekly (Fig. B.3) averaged output data for the 12 scenarios. Fig. 5 and the two Taylor diagrams in Appendix B allow us to compare the ability of each scenario to capture the daily/weekly dynamics of fluxes which is mainly related to weather and weekly/seasonal variability associated to phenology, management events (such as fertilizations, pesticide and irrigation), and drought events, etc. In general, from Fig. 5 and the Taylor diagrams of Appendix B, we noticed similar inter-scenarios differences for daily and weekly scales, as for half-hourly scales, showing (1) the superiority of S2 on MODIS for both NEE and GEE, (2) the better performance of the MV compared to the IV model for R_{ECO} and (3) the better fit when the parameters are optimized per crop type instead of grouping all crop types together. Among the three timescales, Fig. 5 shows that all scenarios driven by MODIS data had higher RSE values (lower model-data fit quality) for daily and weekly scales than for half hourly scale for both NEE and GEE. This indicates the poor capacity of such scenarios driven by MODIS to capture the daily and weekly variability in the cropland CO_2 fluxes which could be associated to weak representation of the phenological variability. On the other hand, S2 derived simulations averaged at daily and weekly time scales for both NEE and GEE were capable of maintaining similar quality of model-data fit than that of half-hourly data. For R_{ECO}, the daily and weekly variabilities for all scenarios were similar to that at the half-hour data with a clear superiority of the MV versus the IV at the three timescales. The three time-scales evaluations for the three fluxes validate the possibility of passing from hourly to daily and weekly scales using the same half hour parameterization while maintaining an acceptable estimation of the three fluxes especially using the S2 data and the MV. Fig. B.4 in Appendix B, shows the RSE calculated at each season separately (winter, spring, summer and autumn). The models' performances per season also follow the same pattern as hourly, daily and weekly time scales with better data-model fitting for S2 compared to MODIS and enhanced simulation of R_{ECO} using the MV model. However, it is noted from Fig. B.4 that spring and summer seasons (usually growing seasons of winter and summer crops) attain higher simulation accuracies in terms of RSE, for the three fluxes, than that obtained in winter and autumn periods (having bare soil conditions corresponding to sowing and harvesting) with lower RSE values than spring and summer for all scenarios.

3.2. Evaluation per crop type

In this analysis, only scenarios driven by the modified version of VPRM were considered since the previous results demonstrated better performance of the MV compared to the standard version. Fig. 6 represents three heat maps of the relative squared error (RSE) calculated for each crop type independently, for the 6 scenarios including EUR_2007 (currently used optimization for ICOS flux maps), MODIS_MV_ALL, MODIS_MV_CropT, S2_MV_ALL, S2_MV_CropT, and the S2_MV_Site. These scenarios are considered as the key scenarios to be analyzed. The EUR_2007 and per site-year scenario (S2_MV_Site) were separated from the four other scenarios for comparison as the first represents an already existing and used optimization and the second has the best fit to the data but is not applicable for upscaling.

The heatmaps of NEE and GEE (Fig. 6a and 6b) clearly show moderate to high RSE values for both MODIS scenarios (ALL and CropT) across all crop types. For example, NEE in MODIS_MV_ALL had high RSE values for maize, oat, potato, barley, and radish (between 0.54 and 0.61) and moderate RSE values of 0.41 and 0.36 for wheat and rapeseed respectively. GEE also showed the same trend with moderate to high RSE values as that of NEE for both MODIS scenarios. The similarity obtained between the EUR_2007 scenario and the two MODIS derived scenarios was expected as the three scenarios (EUR_2007, MODIS_MV_ALL and MODIS_MV_CropT) are based on MODIS vegetation indices and the slight positive difference between our two MODIS scenarios and EUR_2007 could be related to the enhancement provided using the modified VPRM.

For the S2 driven scenarios, the difference in the model-data fit between an optimization mixing all crops (ALL) and a per crop type

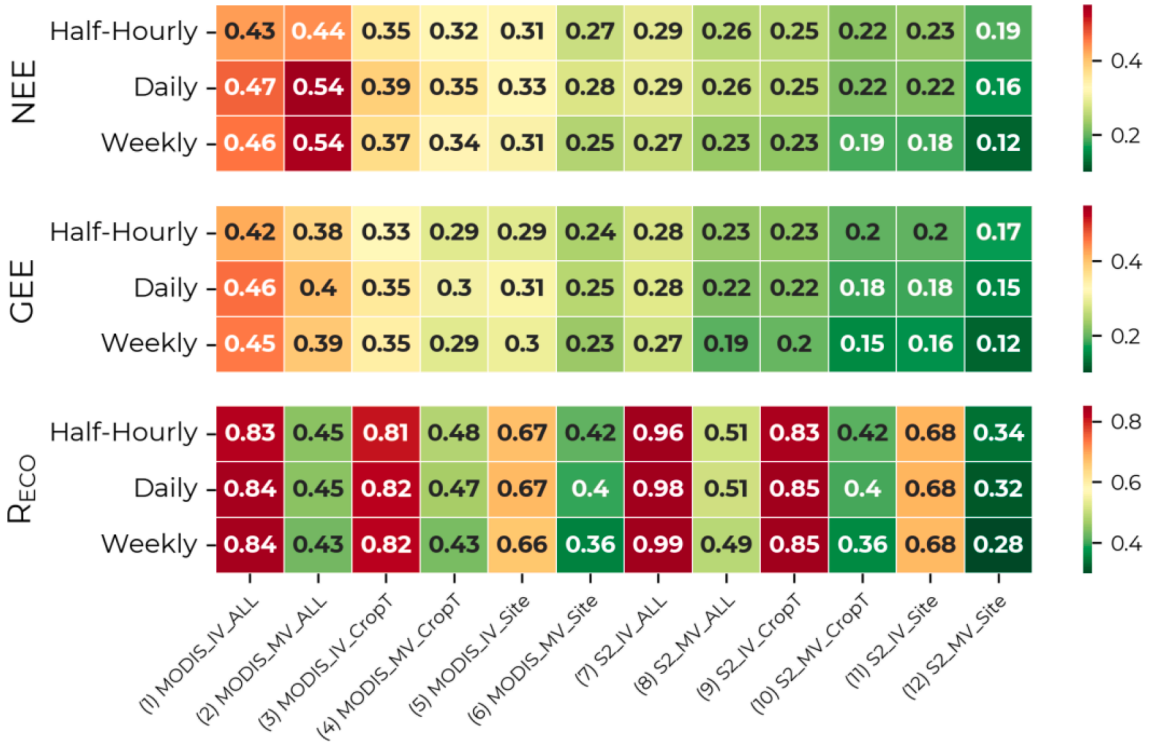

Fig. 5. Heatmap of the variation of the relative squared error (RSE) for the 12 scenarios at half-hourly, daily aggregated and weekly aggregated data.

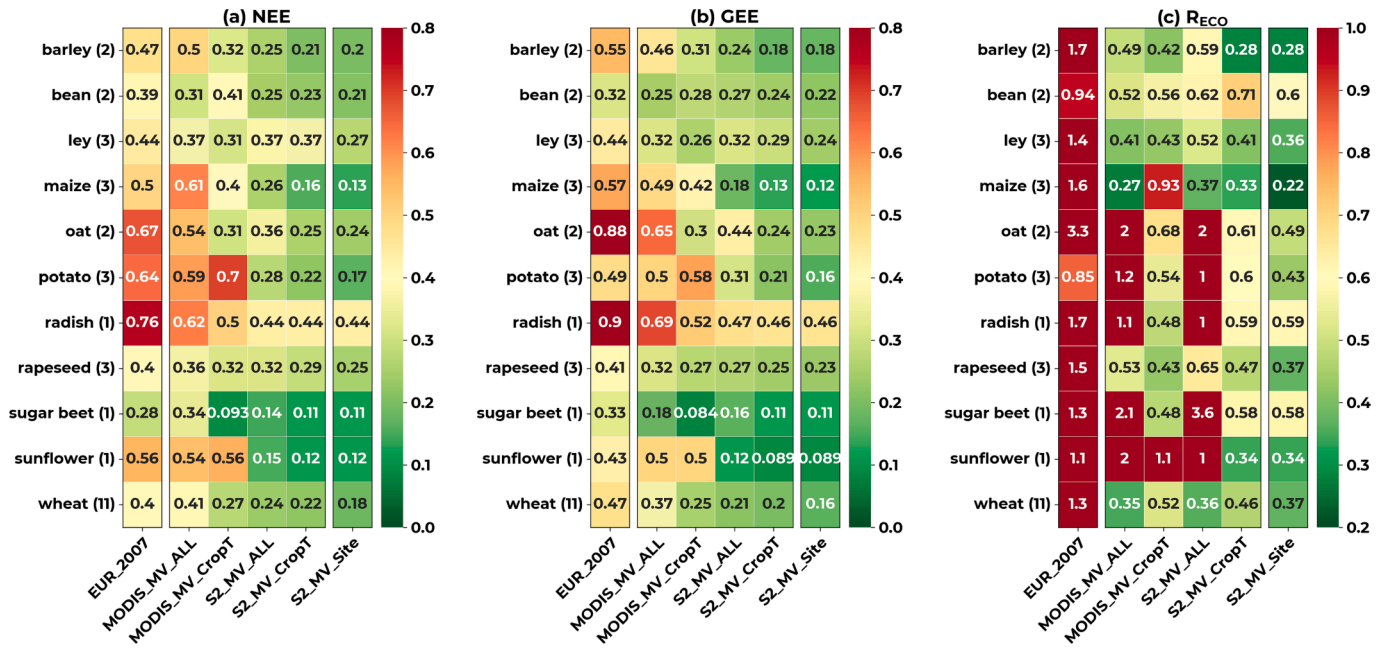

Fig. 6. Heatmap of the variation of the relative squared error (RSE) per crop type for 6 tested scenarios for (a) NEE, (b) GEE and (c) R_{ECO}. The number between parentheses next to each crop type represents the number of available sites-years for this crop type used to calculate the RSE value.

optimization (CropT) was variable according to the crop type. It was noticed from the heatmaps of NEE and GEE (Fig. 6a and 6b) that crop types as barley, maize, oat, sugar beet, potato, and sunflower had significant improvement when applying a specific crop-type based parameterization instead of a generic set of parameters for all crops. For example, the RSE value for maize NEE decreased from 0.26 (0.18 for GEE) using a S2 generic optimization (ALL) to 0.16 (0.13 for GEE) using S2 maize crop parameters. Similarly, the two sites-years with oat crop cover showed a NEE RSE value decreasing from 0.36 (0.44 for GEE) using generic "ALL" optimization to 0.25 (0.24 for GEE) using an oat-crop optimization. On the other hand, wheat crop did not show a significant improvement when using a specific crop type optimization (CropT), and RSE values for both NEE and GEE remained close to those of a generic optimization of all crops (ALL). Despite this limited enhancement between "ALL" and "CropT" for some crops such as wheat, the improvement was variable across different sites-years and could be significant in some cases. For example, Fig. C.1 in Appendix C, representing the RSE values calculated for each site-year for the same scenarios of Fig. 6, shows that for the DE-Rus site having wheat crop in 2018, the RSE of NEE and GEE decreased from 0.22 to 0.15 and from 0.18 to 0.1 respectively when using the wheat-based optimization instead of the generic "ALL" optimization. Similarly, CZ-KrP site in 2020 showed a comparable decrease of from 0.32 to 0.27 in NEE RSE value when using the wheat-based optimization instead of the "ALL".

In general, in the case of S2, the per crop-type optimization (CropT) tends to be closer to the case of a per site-year optimization (Site) than the all-crop optimization (ALL). The current EUR_2007 model used to generate the CO_2 fluxes maps using MODIS and IV by ICOS seems to be significantly less explicit than our S2 "ALL" or "CropT" scenarios. A critical point to consider in this assessment is the variation of the accuracy in the estimation of the ecosystem respiration between S2_MV_ALL and S2_MV_CropT. Generally, Fig. 6c shows that for almost all crop types, the estimation of R_{ECO} was less accurate using ALL than CropT. This can be noticed from the RSE values of the barley, ley, oat, potato, radish, rapeseed, sugar beet, and sunflower where the RSE values largely decreased when using the "CropT" parametrization compared to that using the "ALL" parametrization. Therefore, despite of having acceptable results for both NEE and GEE using the generic optimization (ALL) driven by S2 data and using the MV, the generic parameterization of all crops did not produce a good model-data fit of the R_{ECO} and the per crop-type optimization was more efficient for estimating the three fluxes simultaneously.

3.3. Diurnal cycles

Fig. 7 shows half-monthly composite diurnal cycles (averaged for each hour) for three different crop types including maize in FR-Lam 2019 (Fig. 7a), wheat in DE-RuS 2018 (Fig. 7b), and rapeseed in FR-Aur 2018 (Fig. 7c) calculated for EUR_2007, S2_MV_ALL, S2_MV_CropT and S2_MV_Site key scenarios. For the three site-years, the scenarios showed considerable variations in the models' performances regarding the diurnal variability of net carbon uptake, with a significant variation in the overall magnitude of the diurnal cycle, although they all follow the diurnal trend between day and night. First, the EUR_2007 scenario considerably underestimated the day-time diurnal cycle magnitudes during the whole growing season of maize and wheat with a maximum uptake reaching -12 $\mu molm^{-2}s^{-1}$ and -15 $\mu molm^{-2}s^{-1}$ compared with the observed daytime diurnal magnitude reaching -40 (± 7.95) $\mu molm^{-2}s^{-1}$ and -30 (± 5.7) $\mu molm^{-2}s^{-1}$ for maize (July – August) and wheat (April – May) respectively. For the rapeseed example, the EUR_2007 scenario overestimated the observed daytime diurnal magnitudes especially in the maximum vegetation development stage (between April and June). The EUR_2007 scenario showed low positive and underestimated night-time NEE values indicating lower ecosystem respiration estimation mainly caused by the linear respiration-temperature relation of the IV version, whereas MV based scenarios (ALL or CropT) showed better estimation of the nighttime NEE (positive NEE values) mainly due to better estimation of the ecosystem respiration.

The "CropT" scenario (S2_MV_CropT) in the three examples outperformed the generic scenario (S2_MV_ALL) with daytime NEE values approaching the extreme values of the observed peak daily magnitudes, with less underestimation than the MODIS derived scenarios and the EUR_2007. The closest performance to the observed diurnal cycles was found for the scenario calibrated per crop type (S2_MV_CropT). The green line representing the latter extremely approached, and sometimes laid, within the observational error shaded area for most of the half-monthly diurnal cycles in the three sites especially in the peak

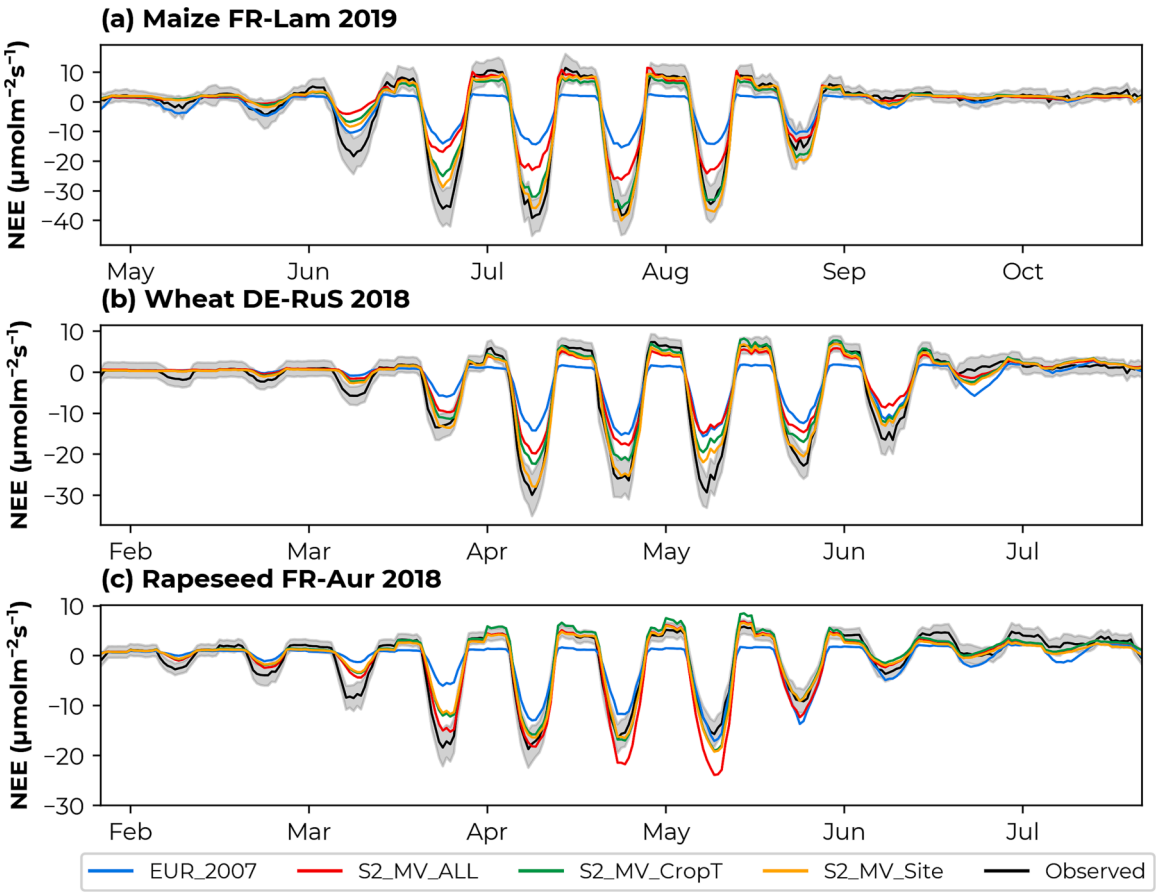

Fig. 7. Examples of half-monthly diurnal cycles during the growing season for (a) maize in FR-Lam 2019, (b) wheat in DE-RuS 2018 and rapeseed in FR-Aur 2018. The shaded region around the observed NEE represents the average observational uncertainty of the measured NEE.

growing season (diurnal cycles of August for maize, April and May for wheat and rapeseed). This reflects the successful reproduction of the diurnal cycle magnitudes using the "CropT" optimization and the superiority of the crop-type based scenario to the generic "ALL" scenario. The peak growing season diurnal cycle presented by Fig. D.1 in Appendix D also guaranteed the same outperformance of the "CropT" with satisfactory predictions of the NEE diurnal cycles.

In general, all the scenarios showed limited capability to reproduce the start of the growing season but then fitted well in the rest of the season. This inadequacy in the beginning of the season could be attributed to the limits in the EVI and LSWI determination (including Pscale and Wscale) when the canopy is not fully covering the soil. In addition, we noticed that even the best data fitting scenario per site-year (S2_MV_Site) could not reach the extreme values of the diurnal cycle in the maximum vegetation development (Fig. 7 and Fig. D.1 in Appendix D). This limitation could be attributed to two main reasons. First, the extremely large flux magnitudes have the highest observational uncertainty values, given that the observational uncertainty increases with the value of the observation, which means less influence of these observations in the weighted least square optimization. Second, this limitation could be due to the possible saturation of the EVI and the incapability to reflect the extreme photosynthetic activity during the full

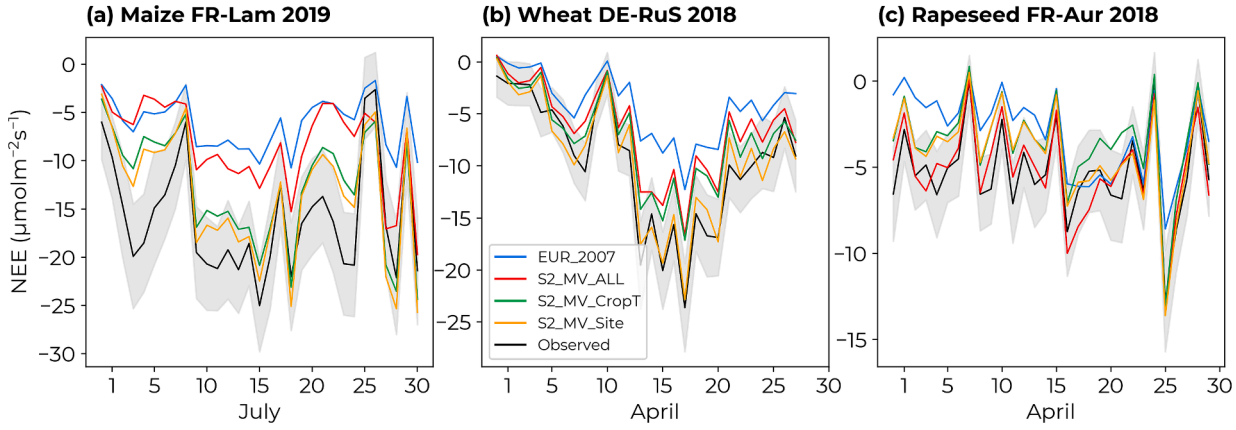

Fig. 8. Daily NEE during the peak growing season of (a) maize crop in FR-Lam 2019, (b) wheat crop in DE-RuS 2018 and rapeseed crop in FR-Aur 2018. The shaded region around the observed NEE represents the average observational uncertainty of the measured NEE.

vegetation development.

Fig. 8 presents the daily mean NEE variability during the peak growing season for the three sites-years above, in July for maize and in April for wheat and rapeseed. For maize, the EUR_2007 and the generic scenarios from S2 (S2_MV_ALL) failed to accurately reproduce the daily variation especially in the peak uptake period between 10 and 20 July 2019 and showed high underestimation of the flux magnitudes. The scenario optimized per crop-type (S2_MV_CropT) had better simulation of the daily variability. This scenario was also capable of capturing the sudden drop in NEE values between 25 and 28 July 2019, which was most probably related to a drought event since temperatures recorded for the period between 23 and 28 July at the flux tower reached its maximum value of July (35 °C) accompanied with the maximum recorded VPD (Vapour-Pressure Deficit) of the month. At the wheat site-year, both the S2_MV_ALL and the S2_MV_CropT captured the daily changes in NEE, similar to that of the rapeseed site-year except for the period between 15 and 20 April where a slight overestimation was observed for S2_MV_ALL compared to S2_MV_CropT for the rapeseed site-year (Fig. 8c).

3.4. Variability in the estimated parameters values

The results presented in the previous sections showed better model-data fit of scenarios calibrated per crop type compared to the generic ALL parameterization using S2. To understand the variability in the performance, Fig. 9 presents the optimized parameters per crop type (CropT) compared to that obtained by the generic (ALL) scenario using S2 data and the modified VPRM (4 GEE parameters and 4 R_{ECO} parameters). Although the average values of all the crop-specific parameters were quite similar to that of the generic (ALL) scenario, the parameters differed significantly between the crop types.

For the GEE, the light use efficiency λ had an average value of 0.32 $\mu molm^{-2}s^{-1}(Wm^{-2})$ for different crop types compared to 0.31 $\mu mol.\ m^{-2}s^{-1}(Wm^{-2})$ for "ALL", with a variation between 0.21 (maize) and 0.67 (oat). The variation of the light use efficiency value across crop types was expected as this parameter is a plant functional-type dependent parameter that relies on temperature and vapor pressure deficit (VPD). $SWRad_0$ values (Wm^{-2}) were less varying across the crop types, except for maize, and attaining a value between 155 Wm^{-2} (ley) and 393 Wm^{-2} (sunflower). Higher $SWRad_0$ value estimated for maize (579 Wm^{-2}) is consistent with the findings of Mahadevan et al. (2008) for maize sites in the USA. The two soil moisture parameters in the GEE (q and θ^*) had larger variability across the crop types. We noticed that the critical soil moisture θ^* for crops such as beans, oat and sugar beet were generally higher than the average value (0.29) and ranged between 0.33 (sugar beet) and 0.63 (oat). Winter crops including wheat, rapeseed, and barley had lower θ^* values than summer crops, ranging between 0.09 (wheat) and 0.24 (rapeseed). The dependency of the R_{ECO} on GEE (unitless parameter k) had an average value of 0.36 among different crops (0.37 for ALL) and varying between 0.23 and 0.57. This average value was slightly higher than that obtained over crop sites in the study of Migliavacca et al. (2011) which was 0.244. The sensitivity of the ecosystem respiration to temperature (E_0) attained an average value of 216.6 (°K) with an "ALL" value reaching 224.3 (°K). However, crops such as radish, bean, barley, and potato showed higher E_0 values compared to the average crop value. The high value of θ_{max} for radish compared to other crops denotes the dependency of this crop on the soil surface wetness. The high variation of all optimized parameters between the "ALL" and the "CropT" confirms that a generic optimization of all crops together could not always generate satisfactory estimation of NEE, GEE and R_{ECO} for all the crop types since each crop attains different crop dependent optimized values.

4. Discussion

4.1. Modified and default VPRM

The modified VPRM presented an improved performance for simulating all three CO_2 fluxes. The evaluation of the IV showed that a simple model with a linear relation between ecosystem respiration and temperature underestimates the amplitude of the R_{ECO} at crop sites and is not appropriate for further applications concerned by the seasonal cycle of global CO_2 and annual carbon balance. Adding both a productivity dependence (GEE) and a soil water content dependence to the R_{ECO} equation in VPRM enhanced the description of R_{ECO}. However, even with the MVPRM, the general moderate accuracy of the R_{ECO}, compared

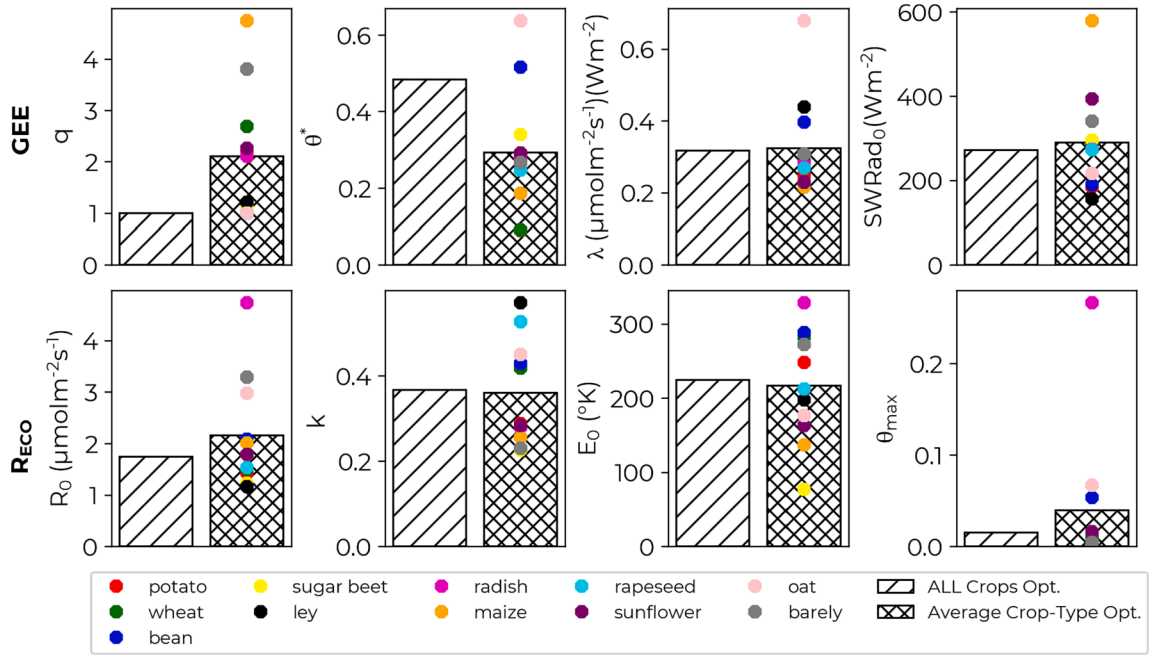

Fig. 9. Optimized parameters for all-crop optimization (ALL) and crop type optimization (CropT) using the S2 vegetation indices and the modified VPRM. Parameters with no units shown on the y-axis are unitless.

to the NEE and GEE, could be related to management impacts in croplands which are not yet explained by the R_{ECO} equation (tillage, fate of crop residues, irrigation etc.). In addition, the low estimation accuracy of R_{ECO} using a generic scenario for all crops together (Fig. 5c and 6c) compared to that obtained using a per crop-type optimization (CropT) could be assigned to the specific crop management associated to each crop type that can be hardly expressed using a generic parametrization for all crops together. A better estimation of R_{ECO} for croplands could be obtained by including crop management drivers especially during the non-growing season such as tillage, cover crops, and the management of crop residues.

The addition of the soil water content function as a driver in the GEE enhanced both GEE and NEE estimates. In fact, the effect of water availability on GEE and R_{ECO} depend on and the magnitude of water stress and the sensitivity of related biotic processes. The modified VPRM for GEE mainly decreased the difference between the measured and simulated standard deviation which implies that the MV better captured the fluctuation in the GEE, which in return could be mainly related to the daily/weekly variations caused by drought events and water stress for croplands. This ensures that with the additional soil moisture driver, the modified VPRM can better simulate GEE values at water stress conditions which was adjusted by the proposed water stress parameter (θ^*) and (q). The limitation in accurate fluxes' estimations in the water stress periods was one of the systematic errors reported by Mahadevan et al. (2008) where sites affected by water stress were less accurately captured by the initial VPRM using only the LSWI as a water stress descriptor.

Nevertheless, for large scale applications, the integration of the soil water content as a driver for both GEE and R_{ECO} requires accurate large scale spatial estimations of the soil moisture at acceptable spatial and temporal resolutions. Current remote sensing-based soil moisture products providing satisfactory soil moisture estimations at several spatial and temporal resolutions include, and are not limited to, the microwave L-band Soil Moisture Active Passive (SMAP) at ~9–30 km spatial resolution (Entekhabi et al., 2010), the enhanced version of SMAP combined with Sentinel-1 product (SMAP-S1) at ~1–3 km spatial resolution (Das et al., 2019) and the Soil Moisture and Ocean Salinity (SMOS) product at ~25 km spatial resolution (Kerr et al., 2001) etc. The global dataset for land components of the European ReAnalysis product (ERA5) (Hersbach et al., 2020, p. 5) provides, in addition to the temperature and shortwave radiation products, the hourly soil moisture estimations at ~9 km spatial resolution which can be used for the large-scale application of the modified VPRM proposed in this study.

4.2. Spatial upscaling using Sentinel-2 vs MODIS

The S2 derived vegetation indices showed considerable improvement in the simulation of the GEE and NEE for crops, especially when using a per crop-type optimization instead of a generic crop optimization for all crop types together. The improvement of GEE and NEE could be mainly related to the finer spatial resolution of S2 which helped reducing the effect of combined reflectance of mixed land cover classes at 500 m scale thus providing an accurate description of the plant phenology independent of the surrounding land cover. Although all sites had approximately pure cropland areas within 500 m around the site according to the S2 dynamic land cover (Table 1), the MODIS derived fluxes showed less model-data fitting accuracy than S2 at site level. To understand this difference between MODIS and S2 in fluxes simulations for croplands, we analyzed the crop-type distribution within the 500 m MODIS pixels for four French sites using the OSO French Land Cover Map (OSO for Occupation des Sols Opérationnelle in French) at 10 m spatial resolution which provides detailed crop-type classification (Inglada et al., 2017) (Table A.0 in Appendix A). These sites could be representative of other European sites. Fig. 10 shows the distribution of land cover classes, including crop types, for the MODIS pixels of the four flux sites in 2018, 2019 and 2020. From Fig. 10 we noticed that most of the flux tower sites had a mixture of different crop types within the 500 m pixel of MODIS. In FR-Aur, FR-Lam and FR-EM2, a mixture of more than 3 crop types are identified in the 500 m MODIS as well as other land

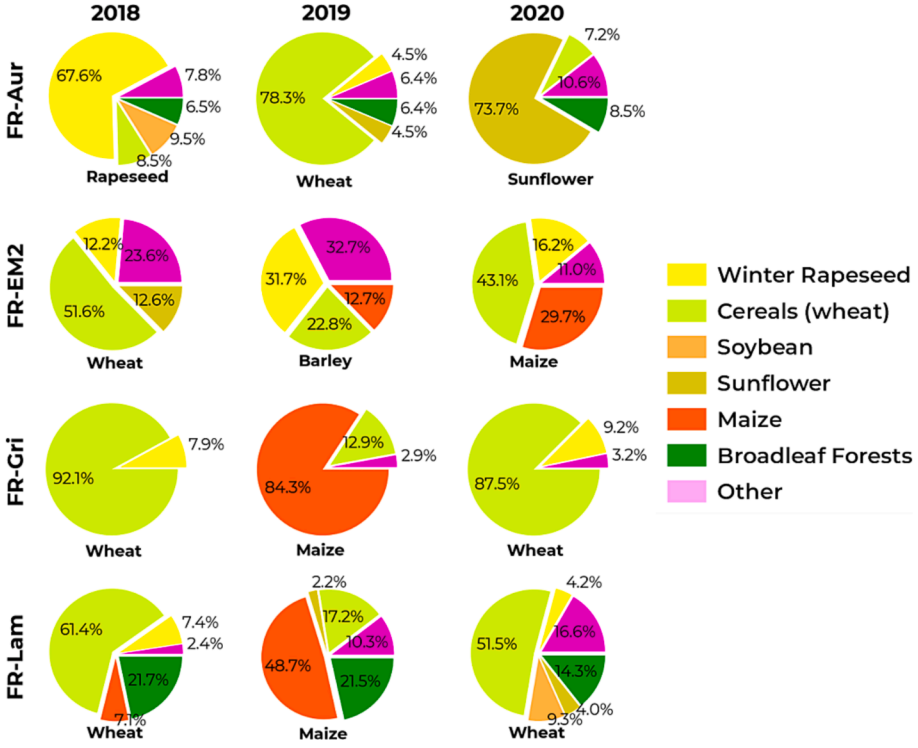

Fig. 10. Distribution of land cover classes within the 500 m pixel of MODIS for four French flux tower sites. Land cover classes are extracted from the yearly OSO French land cover map. Class "Other" includes urban areas, orchards, natural grassland etc. Crop type under each pie chart is the true crop type of the site-year (Table 1).

cover classes (other class stands for urban areas, orchards, natural grassland etc.). The case of FR-Gri showed a dominance of one cop type (more than 85 % single crop) with less heterogeneity but not complete purity. This analysis validates the assumption that the complex heterogeneous features of the cropping system in Europe necessitate fine spatial resolution data for crop CO_2 fluxes and that MODIS vegetation indices may have a mixture of different land cover reflectance that affects the estimation of the cropland CO_2 fluxes in MODIS based scenarios.

To emphasize the importance of using S2 instead of MODIS, and to show the ability to spatially generalize the proposed crop-type parametrization of our propose modified VPRM, we conducted a spatial representation of the CO_2 fluxes over a 30 km x 30 km study site located in the south of France (near FR-Aur flux tower site) at 500 m spatial resolution. We considered the example of wheat crops (common winter crop) where we performed two different CO_2 flux mapping for the year 2019, one using the wheat crop parameters of the MODIS_MV_CropT scenario and the other using the wheat crop parameters of the S2_MV_CropT scenario. MODIS vegetation indices were calculated for the year 2019 for the study site using the MCD43A4 product (same product used for optimization). S2 vegetation indices were extracted only for wheat crops by averaging, within each 500 m pixel, the 10 m S2 pixels corresponding to wheat crops using a wheat crop (cereals) mask from the 10 m French Land Cover Map of the same year (2019). For meteorological data and soil water content, we used the ERA5 dataset that provides hourly temperature, shortwave radiation and soil water content (top first soil layer 0 – 7 cm) at 9 km spatial resolution (see Table A.0 in Appendix A). Finally, GEE was calculated for both MODIS and S2 scenarios using their corresponding wheat parameters and the results were compared with the FR-Aur flux measurements in 2019 (FR-Aur measurement field in 2019 had wheat crop). Besides the objective of showing the difference between S2 and MODIS for CO_2 fluxes upscaling, the second objective here is to test whether the use of spatially continuous meteorological and soil moisture datasets for large scale applications, such as that of ERA5, would affect the estimations accuracies.

Fig. 11 shows examples of daily averaged GEE over a study site near FR-Aur flux tower (Fig. 11a) calculated using S2_MV_CropT and MODIS_MV_CropT (Fig. 11b) for winter wheat (cereals) crops. Daily examples are taken at day of year (DOY) 60, 90, 120, 150 and 180 during the wheat growing season. The GEE maps of MODIS and S2 clearly showed the underestimation of the MODIS derived GEE compared to that estimated from S2 especially in the peak growing season (DOY 120 and DOY 150). While MODIS GEE saturated in the peak growing season at an order of 10 to 15 $\mu molm^{-2}s^{-1}$, S2 provided higher estimation reaching an order of 20–25 $\mu molm^{-2}s^{-1}$. This underestimation of MODIS GEE is most likely due to lower magnitude of vegetation indices of MODIS pixels having a mixture of either other crop types or bare soil fields within the 500 m resolution (summer crops are usually bare soil in winter. At the end of the wheat crop cycle (DOY 180), MODIS GEE estimations showed higher values than that for S2 having lower GEE values representing the possible harvest (end of cycle). These high values by MODIS at the end of the wheat growth cycle could probably be due to the contribution of the summer crops in the MODIS EVI and LSWI values within the 500 m spatial resolution of MODIS pixels (starting season of summer crops in May-June). The scatter plots of the comparison of hourly estimated GEE for both MODIS and S2 with FR-Aur flux measurements (Fig. 11c) show that MODIS GEE underestimated the measured GEE values with an RMSE reaching 4.90 $\mu molm^{-2}s^{-1}$ compared to 3.55 $\mu molm^{-2}s^{-1}$ for the S2 derived GEE. The comparison between the spatially upscaled S2 GEE and the measured GEE in Fig. 11c demonstrates that the use of ERA 5 data for temperature, shortwave radiation and soil water content in the spatial upscaling did not highly affect the estimation accuracy. Indeed, the flux site FR-Aur in 2019 had an optimization accuracy reaching 0.17 by means of RSE (using flux meteorological data and soil moisture) which slightly decreased to 0.19 using the ERA-5 forced estimations. This guarantees the capacity of generalizing the crop-type optimized MVPRM at large scales using spatially continuous meteorological and soil moisture data such as that provided by the ERA5.

To understand the lower GEE values simulated by MODIS compared to S2 in the peak growing season and higher values at the end of the wheat crop cycle, Fig. E.1. in Appendix E presents the time series of both EVI and LSWI derived from S2 and MODIS and averaged over all 500 m sub-pixels in the study zone. The EVI time series shows that MODIS EVI reached a maximum value of 0.47 $\pm$ 0.10 less than that of S2 that reached 0.61 $\pm$ 0.12 in the peak growing season. Moreover, MODIS derived EVI and LSWI showed higher values than S2 for the period between June and August 2019. Fig. E.2a in Appendix E presents the distribution of the land cover classes within the study area while Fig. E.2b shows the percentage of MODIS pixels as a function of the wheat area percentage within each 500 m pixel. While wheat is the dominant crop type in the study site (29 %), sunflower crop represents about 17 % of the land cover classes followed by urban areas (15 %) and grassland (12 %). Sunflower and urban areas contributing to the MODIS 500 m spectral reflectance probably reduced EVI values in the peak growing season (in spring) where sunflower (summer crops) are bare soil and urban areas usually have very low EVI values. In summer (end of wheat crop cycle), the sunflower crop cycle starts and higher EVI values for MODIS was obtained probably due to the contribution of the sunflower crop cover in the MODIS surface reflectance. Analyzing the wheat area percentage within the 500 m pixels (Fig. E.2b), we noticed that about 36 % of the 500 m pixels in the study site had less than 20 % of wheat areas whereas only 33 % of the pixels had more than 40 % pure wheat area. These findings confirm the assumption that the 500 m spatial resolution of MODIS could not be always adequate for European cropping systems with heterogeneous features, complex rotations and small farmland properties. In an estimation of the global distribution of the agricultural fields sizes, Lesiv et al. (2019) showed that in the European agricultural areas, fields' sizes are either small (between 0.64 and 2.56 ha) or medium (between 2.56 and 16 ha) which is less than the size of one MODIS pixel (25 ha).In addition, according to the European statistics of farmland, about 63.8 % of the European agricultural holdings are less than 5 ha (Farms, nd) . Consequently, the diversity of the land cover types, and the small sized European farms compared to the 500 m spatial resolution of MODIS led to less accurate representation of the vegetation phenology and inadequate estimation of the GEE and NEE.

For larger scale applications of crop-type optimized MVPRM (i.e., European scale), crop type land cover maps at fine spatial resolution are required to distinguish between different crop types. Where at the French scale we used the French land cover map which includes detailed recognition of several crop types (as shown in Figs. 10 and 11), at the European scale the current advances in machine learning demonstrated the capability of obtaining quite accurate crop type classification maps at fine spatial resolution. A recent study by d'Andrimont et al. (2021) proposed the first 10-m crop type map for the European Union for nineteen (19) crop types developed using the RF classification and based on the Sentinel-1 time series data. Such dataset is sufficient to produce CO_2 flux maps for each crop type using the crop-type parameterization provided in this study at the European Union scale. With the near-real-time availability of Sentinel-2 data, future work will concentrate on establishing a continuous monitoring system for cropland CO_2 fluxes at national and continental scales, enabling quasi-real-time tracking at high spatial resolution. A detailed and accurate spatial representation of cropland CO_2 fluxes would aid in the precise monitoring of crop health in near real-time, the analysis and assessment of the impact of extreme events such as droughts and heatwaves on crop yields, and the forecasting of crop yields during the growing season. Future work will also focus on enhancing the VPRM equation to consider more drivers for cropland CO_2 fluxes, including crop management practices such as tillage, harvest, fertilization, and irrigation. Despite optimizing the

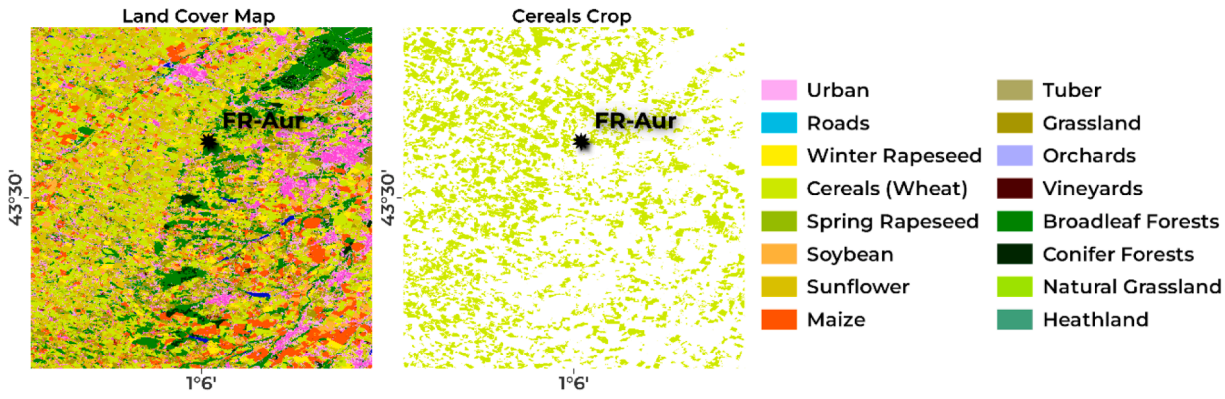

(a)

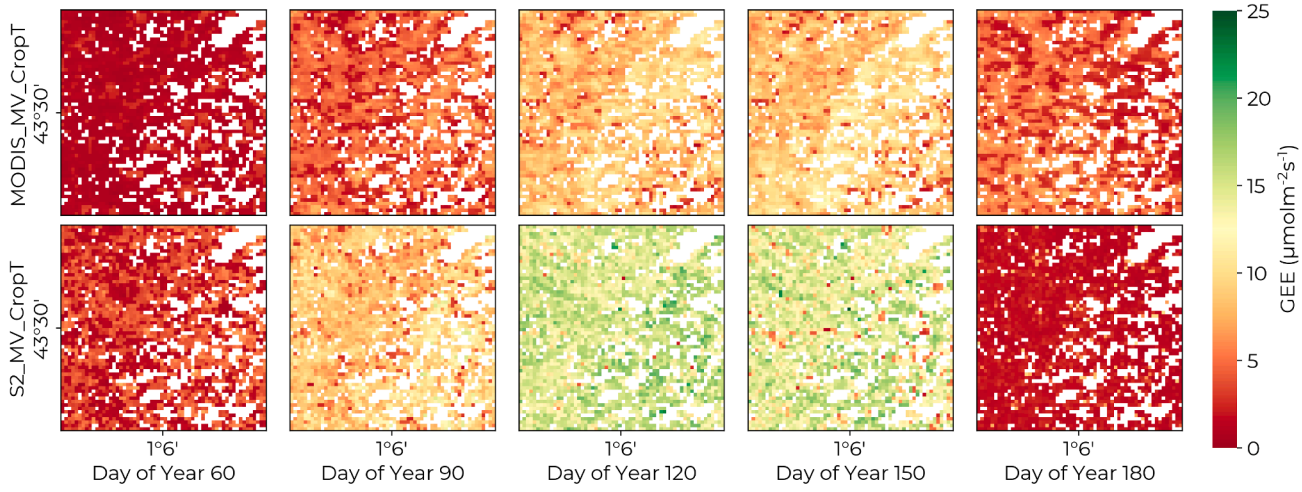

(b)

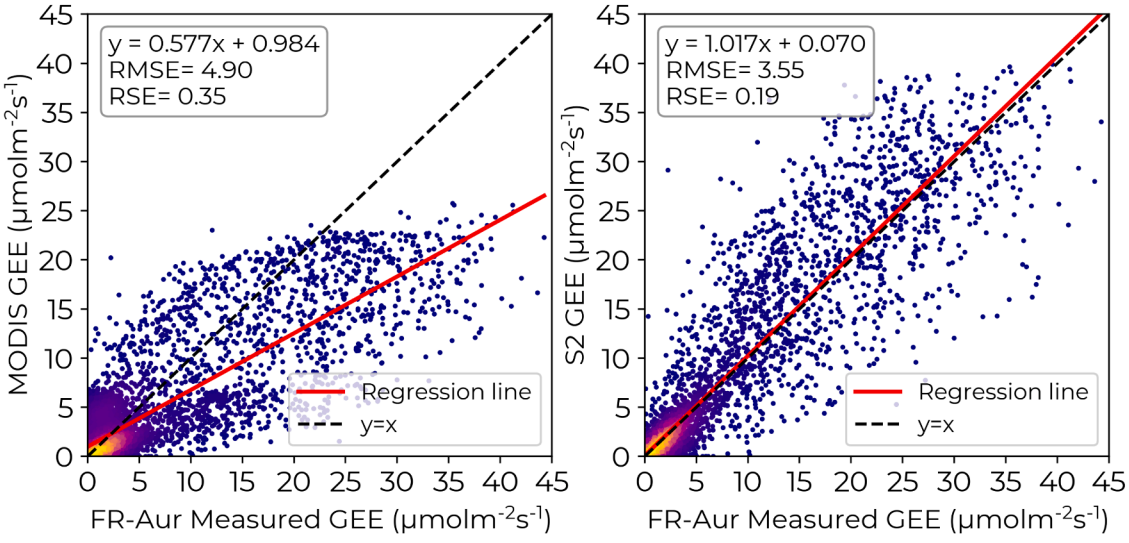

(c)

Fig. 11. Example of the application of the S2_MV_CropT and MODIS_MV_CropT optimizations on wheat (cereals) in south France using the ERA-5 meteorological and soil moisture data. (a) the study site near FR-Aur flux tower (30 km x 30 km) with the corresponding land cover map and cereals mask in 2019. (b) Daily aggregated examples of estimated GEE for wheat using MODIS and S2 at 500 m spatial resolution for selected days of years during the wheat cycle. White areas in GEE maps represent 500 m pixels having no cultivated wheat in 2019 according to the land cover map. (c) Density scatter comparing the hourly estimated and measured GEE at the FR-Aur flux tower in 2019 for both S2_MV_CropT and MODIS_MV_CropT optimizations.

VPRM and MVPRM using site scale meteorological and soil moisture data, the use of the ERA5 data for meteorological data as well as the soil moisture estimates proved to be efficient for large scale mapping of CO_2 fluxes as shown in the upscaling example. However, the use of the SWRad in the GEE equations instead of the PAR can induce potential uncertainties. In the VPRM as well as the MVPRM equations for GEE, PAR was replaced by SWRad since, unlike PAR, the SWRad is usually available operationally at large scales through meteorological datasets such as the ERA5. Although PAR is proportional to the SWRad with PAR being about 45 % of the SWRad (Howell et al., 1983), this value can vary from 42 % to 59 % depending on the weather conditions (cloudiness and solar angles). Under cloudy conditions, Zhang et al. (2020) showed that larger GEE could be observed in the morning and afternoon mainly due to higher diffuse PAR fraction whereas larger GEE in midday could be due to lower temperature and VPD. In such cloudy conditions, shaded leaf photosynthesis could be limited by light, but the diffuse light can increase GEE. Therefore, the assumption of a direct linear relationship between PAR and SWRad can be limited for such cloudy conditions and may induce potential uncertainty in the upscaling.

5. Conclusion

We proposed a modification of the VPRM model to improve the simulation of cropland CO_2 fluxes in Europe. Modifications of the VPRM included first the replacement of the commonly used MODIS vegetation indices at 500 m spatial resolution by the Sentinel-2 vegetation indices at 10 m spatial resolution to address the complex heterogenic feature of the European cropping system. Second modification incorporated the addition of soil moisture functions to the GEE and R_{ECO} equations to account for water stress effects on both fluxes. Contrary to the conventional assumption of having one set of parameters for all crop types in the initial VPRM, the study proposed to optimize crop-type specific parameters for common crops in Europe. Modified VPRM parameters were optimized using eddy covariance measurements at selected European cropland flux sites comprising 11 different crop types. Main results showed that the use of S2 vegetation indices in the modified VPRM better simulated the three CO_2 fluxes (NEE, GEE and R_{ECO}) especially in the peak growing season whereas MODIS underestimated the CO_2 fluxes for most crop types. Compared to a single parameterization of all crops together, the crop-specific parametrization of the modified VPRM enhanced the simulations of CO_2 fluxes obtaining lower RMSE and RSE values for several crops including maize, oat, sugar beet and barley. The addition of the soil moisture functions in both GEE and R_{ECO} allowed better simulations of the CO_2 fluxes in drought periods illustrated by better fitting of the daily/weekly fluxes' fluctuations caused by drought events. The modified R_{ECO} equation better fitted the ecosystem respiration than the simple respiration-temperature linear function used in the initial VPRM for all crop types. An example of a spatial upscaling of the CO_2 fluxes for wheat crops, using the modified VPRM, detailed crop type land cover map and ERA 5 data for soil moisture, demonstrated the superiority of S2 over MODIS. Using MODIS data, the mixture of different land cover classes in the 500 m spatial resolution of MODIS revealed less accurate fluxes' estimations than the high resolution S2 data. With less accuracy obtained for R_{ECO} compared to NEE and GEE, future work will concentrate on better improving the cropland R_{ECO} equation by considering crop management effects on the vegetation respiration. Future work will also concentrate on producing high resolution cropland CO_2 flux maps over the European continent using S2 and the crop-type parameterized modified VPRM.

Funding

This work has benefited from the French State aid managed by the National Research Agency (ANR) under the Program of "Investments of the Future" with the reference ANR-16-CONV-0003. The work received support of ATOS France and ANR, via the contract S40072 under the "Plan France Relance".

CRediT authorship contribution statement

Hassan Bazzi: Conceptualization, Data curation, Formal analysis, Methodology, Software, Writing – original draft. **Philippe Ciais:** Conceptualization, Data curation, Formal analysis, Methodology, Writing – review & editing. **Ezzeddine Abbessi:** . **David Makowski:** . **Diego Santaren:** Methodology, Validation, Writing – review & editing. **Eric Ceschia:** Data curation, Resources. **Aurore Brut:** Data curation, Resources. **Tiphaine Tallec:** . **Nina Buchmann:** . **Regine Maier:** Resources. **Manuel Acosta:** Resources, Writing – review & editing. **Benjamin Loubet:** Resources, Writing – review & editing. **Pauline Buysse:** Resources. **Joël Léonard:** Resources. **Frédéric Bornet:** Resources. **Ibrahim Fayad:** Writing – review & editing. **Jinghui Lian:** . **Nicolas Baghdadi:** Writing – review & editing. **Ricard Segura Barrero:** Resources, Data curation. **Christian Brümmer:** . **Marius Schmidt:** Data curation, Resources. **Bernard Heinesch:** Data curation, Resources. **Matthias Mauder:** Data curation, Resources. **Thomas Gruenwald:** Data curation, Resources.

Declaration of competing interest

The authors declare that they have no known competing financial interests or personal relationships that could have appeared to influence the work reported in this paper.

Data availability

Data will be made available on request.

Acknowledgements

The authors would like to thank the CLAND convergence institute and the French National Research Agency (ANR) for supporting this work. Authors would like also to thank the Integrated Carbon Observation System (ICOS) and FLUXNET for providing eddy covariance data. The Czech site would like to thank the Ministry of Education, Youth and Sports of Czech Republic within the CzeCOS program for the funding support, grant number LM2023048.

Appendix A

Summary table of data used in this study with their corresponding data source

Data	Description	Source
Eddy Covariance Data	Half hourly CO_2 flux measurements at flux towers (footprint ~ 150 m)	https://www.icos-cp.eu/data-products https://fluxnet.org/data/fluxnet2015-dataset/fullset-data-product/
S2 Dynamic Land Cover	10 m near-real-time (NRT) Land Use/Land Cover (LULC) dataset that includes class probabilities and label information for nine classes	https://developers.google.com/earth-engine/datasets/catalog/GOOGLE_DYNAMICWORLD_V1

(*continued on next page*)

(*continued*)

Data	Description	Source
MCD43A4.061 MODIS	Daily Nadir Bidirectional Reflectance Distribution Function Adjusted Reflectance (NBAR) product at 500 m spatial resolution. Combines data from both the Terra and Aqua spacecrafts, choosing the best representative pixel from the 16-day period	https://developers.google.com/earth-engine/datasets/catalog/MODIS_061_MCD43A4
Sentinel-2 Level-2A	~ 5 to 10 days cloud free optical images at 10 m spatial resolution. BRDF corrected using (Roy et al., 2017) adjustment	https://developers.google.com/earth-engine/datasets/catalog/COPERNICUS_S2_SR
ERA5-Reanalysis	Half hourly meteorological data and soil moisture estimations at ~ 9 km spatial resolution	https://cds.climate.copernicus.eu/cdsapp#!/search?type=dataset
French Land Cover Map	Classified land cover map of France including 23 different classes and 11 different crop types	https://www.theia-land.fr/en/product/land-cover-map/

where ρ_{NIR}, ρ_{Red}, ρ_{Blue} and ρ_{SWIRed} are the near infrared, red, blue and the shortwave infrared bands respectively. For Sentinel-2, the ρ_{NIR} , ρ_{Red}, ρ_{Blue} and ρ_{SWIRed} correspond to bands B8, B4, B2 and B11 respectively.

Enhanced Vegetation Index (EVI) $$EVI = \frac{2.5 \times (\rho_{NIR} - \rho_{Red})}{(\rho_{NIR} + 6 \times \rho_{Red} - 7.5 \times \rho_{Blue} + 1)} \quad \text{A.1}$$

Land Surface Water Index (LSWI) $$LSWI = \frac{\rho_{NIR} - \rho_{SWIRed}}{\rho_{NIR} + \rho_{SWIRed}} \quad \text{A.2}$$

Temperature scale(T_{scale}) $$T_{scale} = \frac{(T - T_{min}) \times (T - T_{max})}{\left[(T - T_{min})(T - T_{max}) - \left(T - T_{opt}\right)^2\right]} \quad \text{A.3}$$

Tmin (5 °C), Tmax (40 °C) and Topt (22 °C) are the minimum, maximum and optimal temperatures for photosynthesis in croplands respectively and fixed at literature values.

Water Scale (W_{scale}) $$W_{scale} = \frac{1 + LSWI}{1 + LSWI_{max}} \quad \text{A.4}$$

Phenology Scale (P_{scale}) $$P_{scale} = \frac{1 + LSWI}{2} \quad \text{A.5}$$

P_{scale} was calculated as in equation A.5 from bud burst to leaf full expansion, then considered as a value of "1″ after the leaf full expansion until the senescence phase where equation A.5 is reapplied. The three phenology phases were identified using a simple EVI seasonal thresholding.

Correlation coefficient (r) $$r = \frac{\sum_{i=1}^{n}(y_i - \overline{\widehat{y}})(\widehat{y}_i - \overline{\widehat{y}})}{\sqrt{\sum_{i=1}^{n}(y_i - \overline{\widehat{y}})^2}\sqrt{\sum_{i=1}^{n}(\widehat{y}_i - \overline{\widehat{y}})^2}} \quad \text{A.6}$$

Standard deviation of the measured fluxes (SD_m) $$SD_m = \sqrt{\frac{\sum_{i=1}^{n}(y_i - \overline{y})}{N}} \quad \text{A.7}$$

Standard deviation of the simulated fluxes (SD_s) $$SD_s = \sqrt{\frac{\sum_{i=1}^{n}(\widehat{y}_i - \overline{\widehat{y}})}{N}} \quad \text{A.8}$$

Root Mean Squared Error (RMSE) $$RMSE = \sqrt{\frac{\sum_{i=1}^{n}(y_i - \widehat{y}_i)^2}{N}} \quad \text{A.9}$$

Relative Squared Error (RSE) $$RSE = \frac{\sum_{i=1}^{n}(y_i - \widehat{y}_i)^2}{\sum_{i=1}^{n}(y_i - \overline{y})^2} \quad \text{A.10}$$

AIC $$AIC = Nln\left(\frac{\sum_{i=1}^{n} w_j^{-2}(y_i - \widehat{y}_i)^2}{N}\right) + 2(p+1) \quad \text{A.11}$$

Squared Bias (SB) $$SB = (\overline{y} - \overline{\widehat{y}})^2 \quad \text{A.12}$$

SDSD $$SDSD = (SD_s - SD_m)^2 \quad \text{A.13}$$

LCS $$LCS = 2SD_sSD_m(1 - r) \quad \text{A.14}$$

where y_i is the measured flux value, $\widehat{y}_i$ is the simulated flux value, $\overline{y}$is the mean of the measured flux values, $\overline{\widehat{y}}$is the mean of the simulated flux values, N is the total number of simulated flux values, w_j is the flux observation uncertainty and p is the number of optimized parameters.

Appendix B

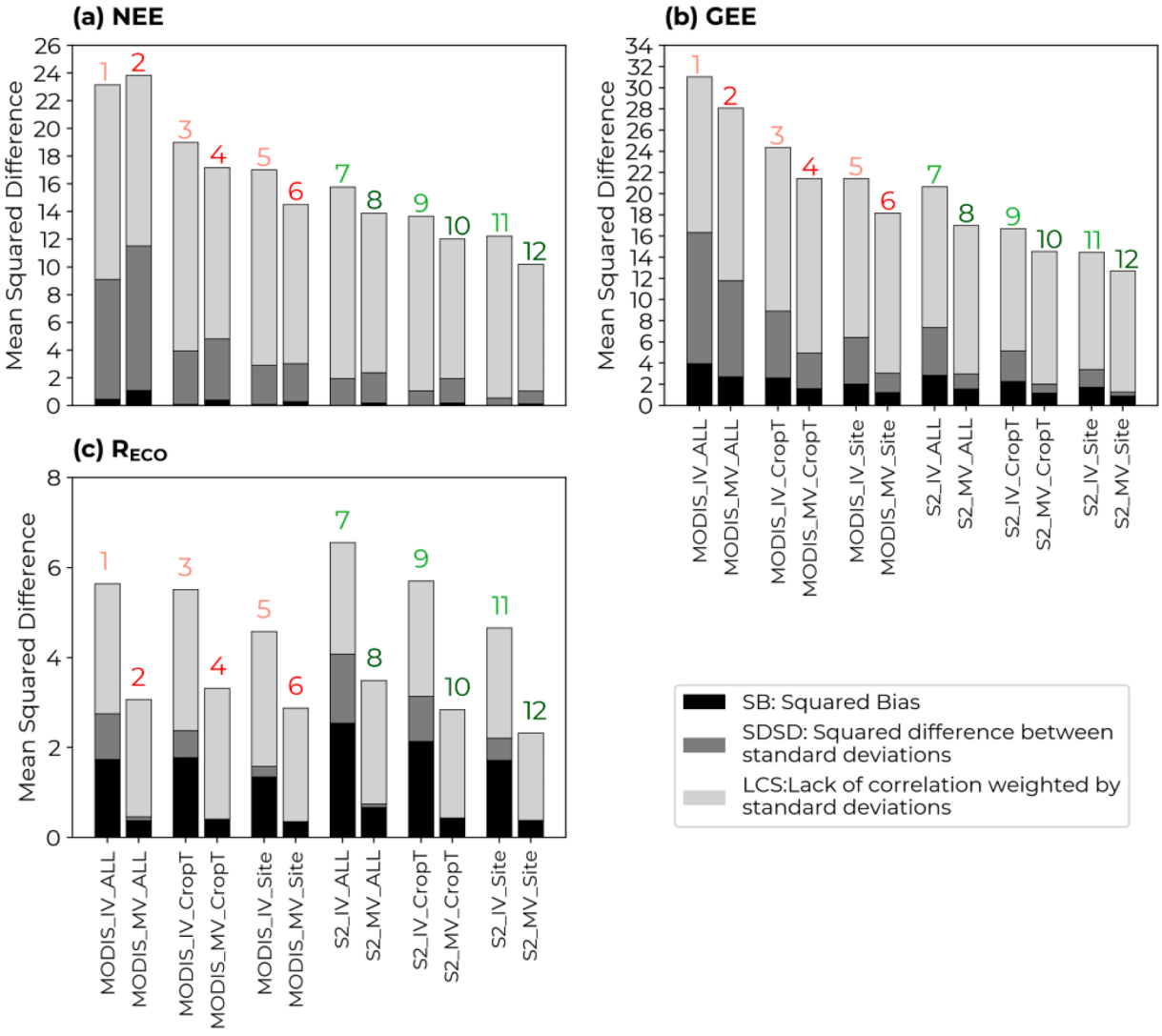

Fig. B1. Mean squared deviation (MSD) and its components squared bias (SB), squared difference between measured and simulated standard deviations (SDSD) and lack of correlation weighted by standard deviation (LCS) for the 12 scenarios calculated using half hourly data. Numbers over bars represent the scenario numbers (SN) shown in Table 2. (a) NEE, (b) GEE and (c) R_{ECO}.

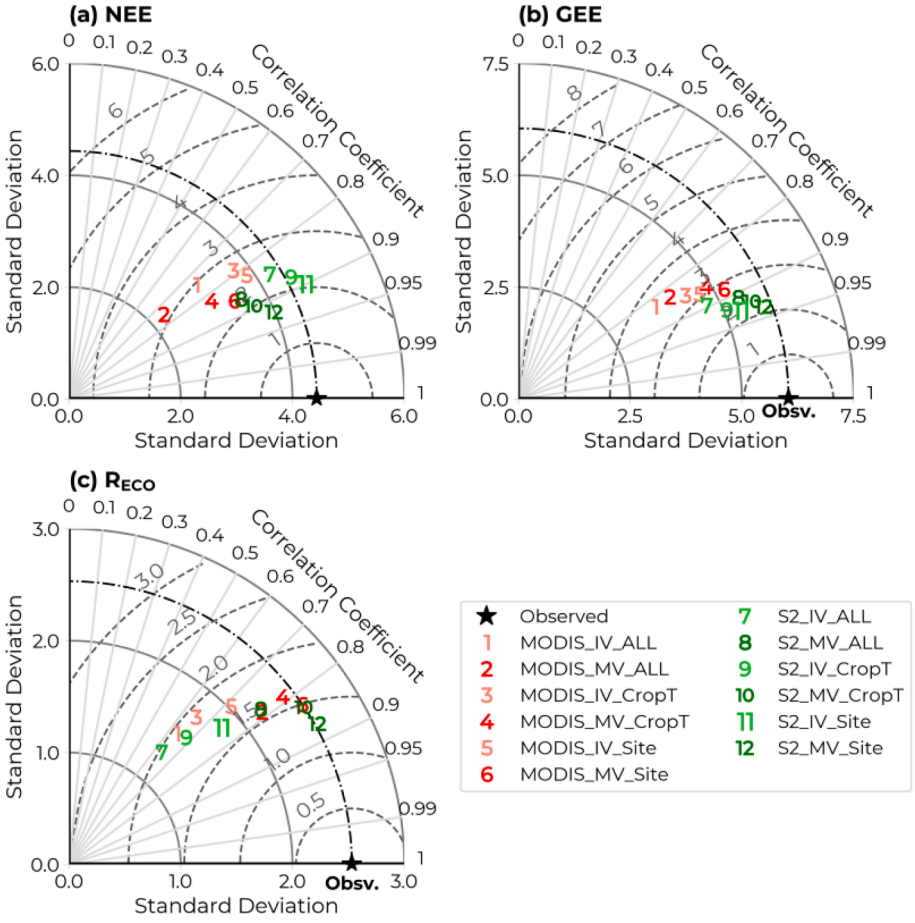

Fig. B2. Taylor Diagram for the 12 tested scenarios for aggregated daily data. (a) NEE, (b) GEE and (c).R_{ECO}

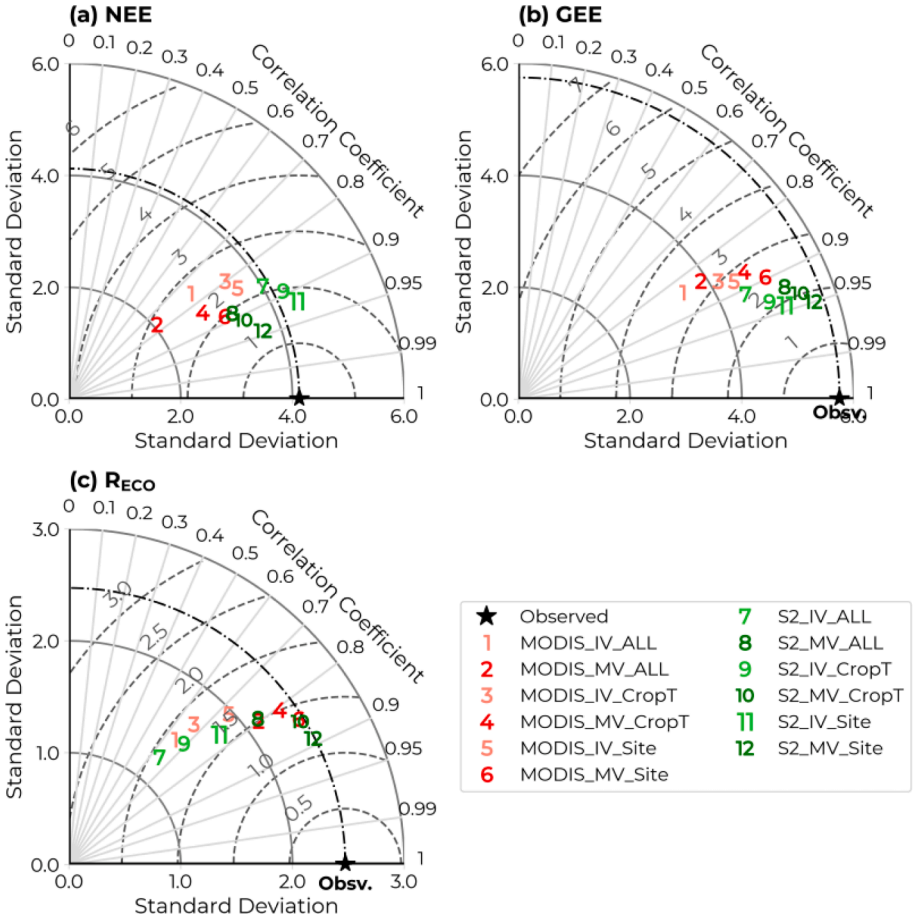

Fig. B3. Taylor Diagram for the 12 tested scenarios for aggregated weekly data. (a) NEE, (b) GEE and (c).R_{ECO}

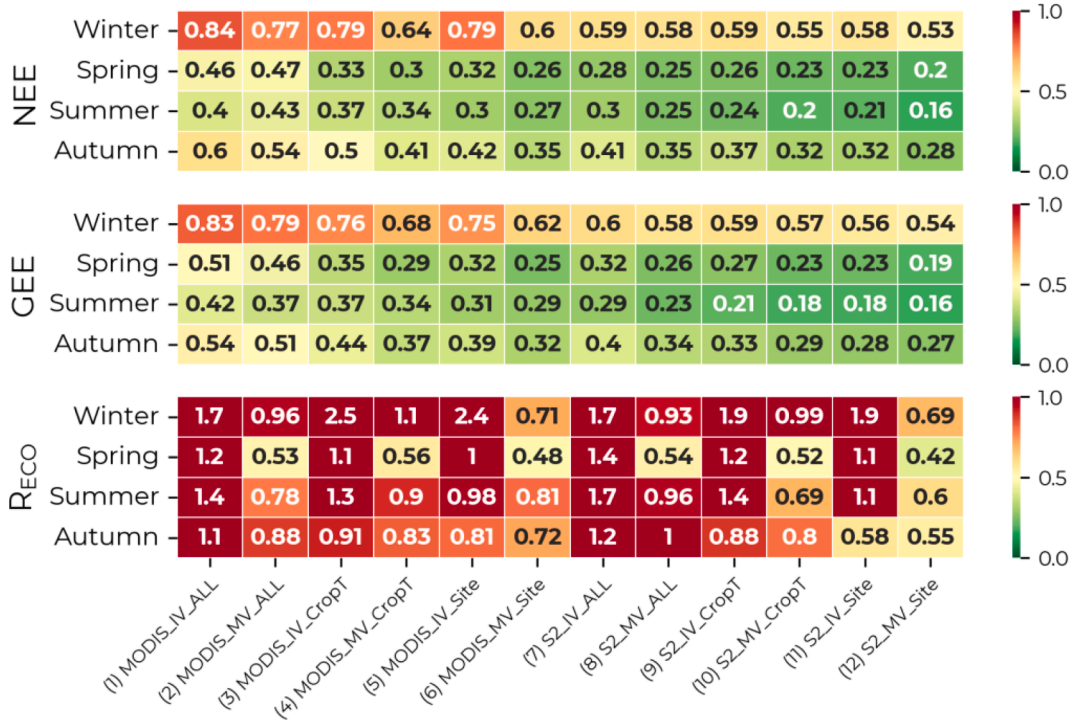

Fig. B4. Heatmap of the variation of the relative squared error (RSE) per season for the 12 scenarios. Winter: December-January-February, Spring: March-April-May, Summer: June-July-August, Autumn: September-October-November).

Appendix C

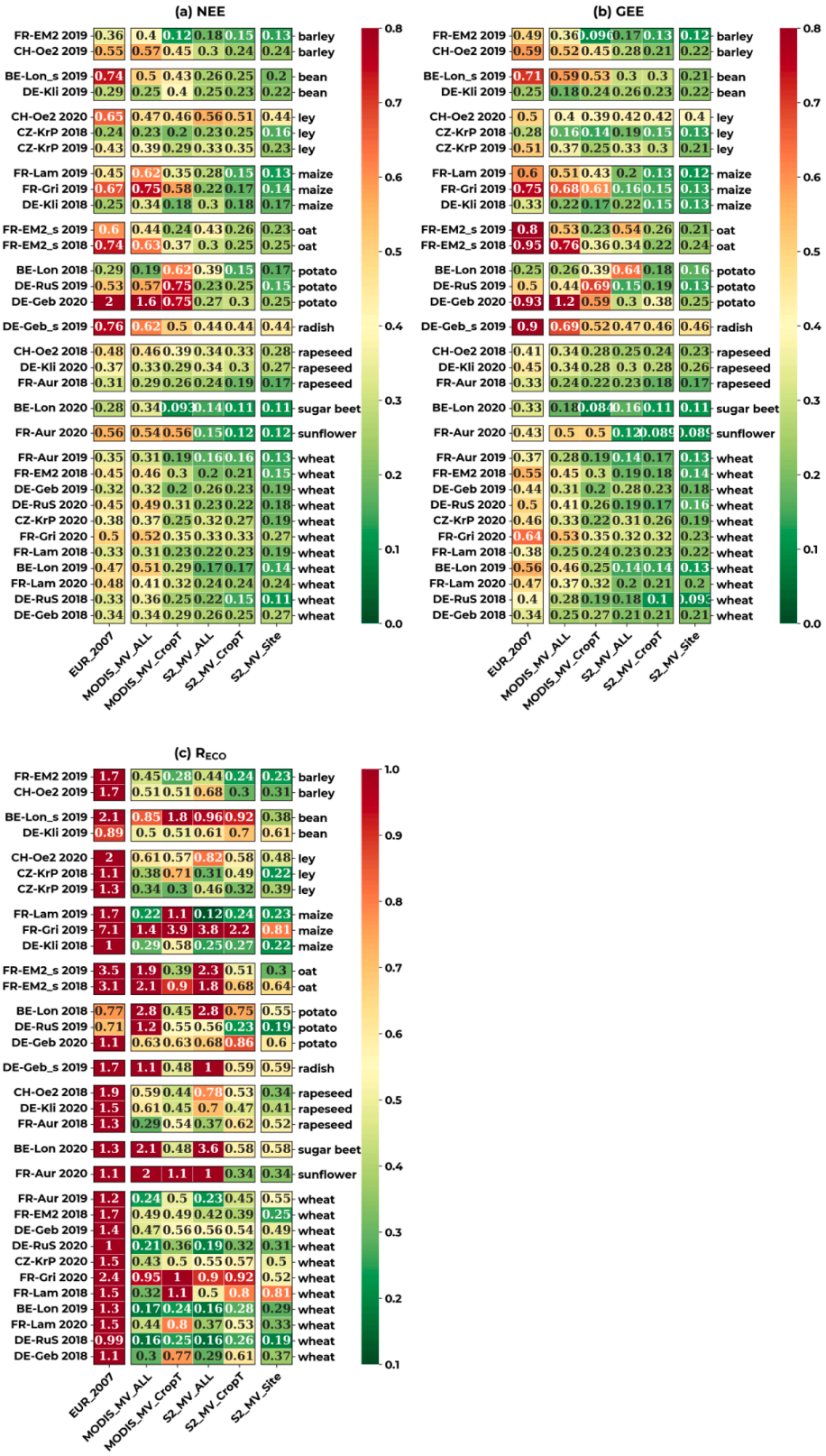

Fig. C1. Heatmap of the variation of the relative squared error (RSE) per site-year for 6 tested scenarios. (a) NEE, (b) GEE and (c).R_{ECO}

.

Appendix D

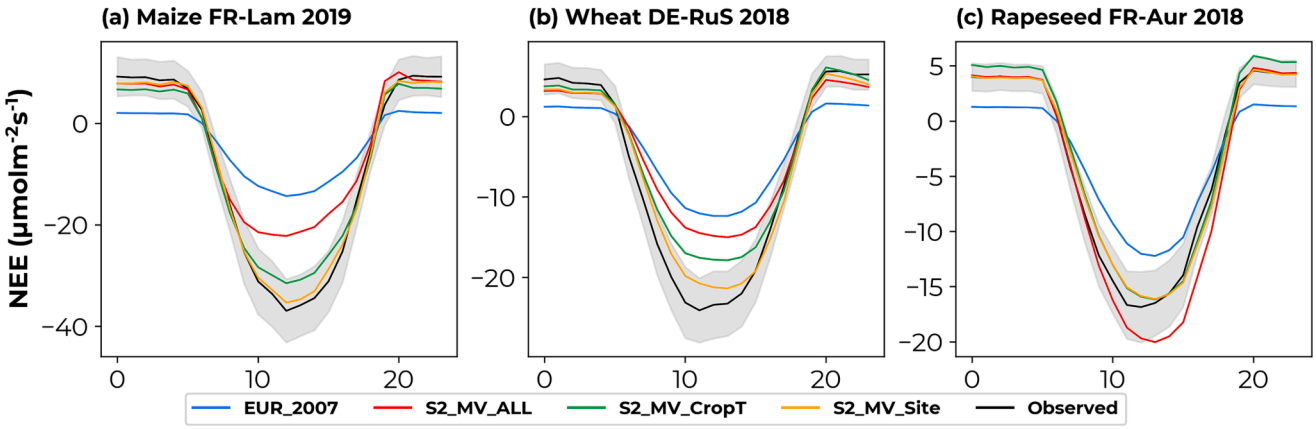

Fig. D1. Peak growing season diurnal cycles of (a) maize crop in FR-Lam 2019, (b) wheat crop in DE-RuS 2018 and rapeseed crop in FR-Aur 2018. x-axis represents the hour.

Appendix E

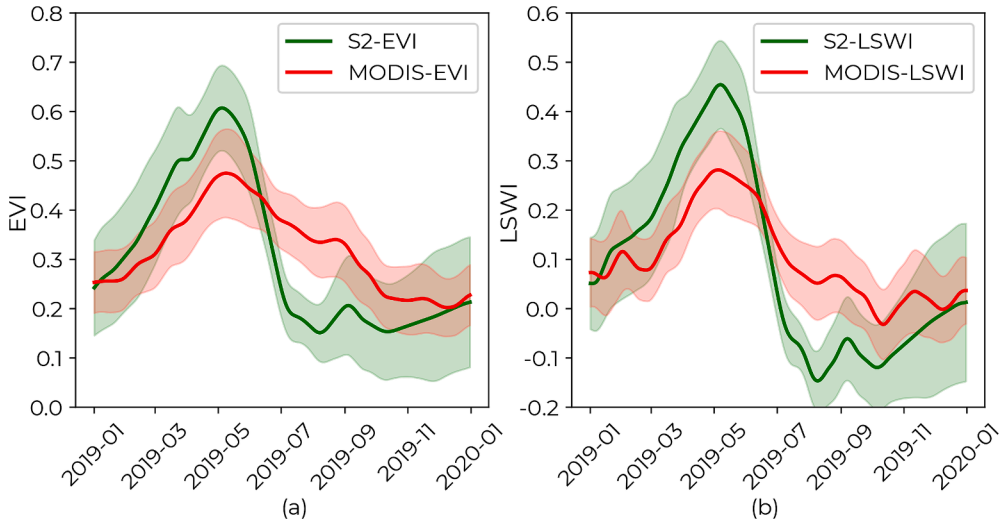

Fig. E1. Time series of the average EVI (a) and LSWI (b) for 500 m pixels derived using S2 (green) and MODIS (red) data at the upscaling study site (30 km x 30 km). Shaded region corresponds to the standard deviation of the calculated average of all 500 m pixels.

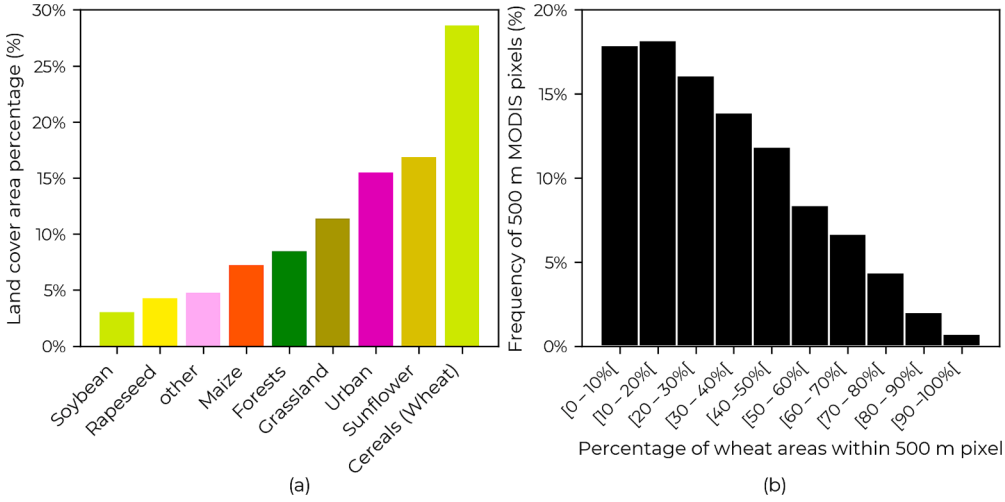

Fig. E2. (a) Percentage of the land cover classes within the upscaling study site (30 km x 30 km) and (b) the frequency of the MODIS pixels as a function of the wheat area percentage within the 500 m pixel.

References

Akaike, H., 1974. A new look at the statistical model identification. IEEE Trans. Automat. Contr. 19, 716–723. https://doi.org/10.1109/TAC.1974.1100705.

Banks, H.T., Joyner, M.L., 2017. AIC under the framework of least squares estimation. Applied Mathematics Letters 74, 33–45. https://doi.org/10.1016/j.aml.2017.05.005.

Battude, M., Al Bitar, A., Morin, D., Cros, J., Huc, M., Marais Sicre, C., Le Dantec, V., Demarez, V., 2016. Estimating maize biomass and yield over large areas using high spatial and temporal resolution Sentinel-2 like remote sensing data. Remote Sensing of Environment 184, 668–681. https://doi.org/10.1016/j.rse.2016.07.030.

Beer, C., Reichstein, M., Tomelleri, E., Ciais, P., Jung, M., Carvalhais, N., Rödenbeck, C., Arain, M.A., Baldocchi, D., Bonan, G.B., Bondeau, A., Cescatti, A., Lasslop, G., Lindroth, A., Lomas, M., Luyssaert, S., Margolis, H., Oleson, K.W., Roupsard, O., Veenendaal, E., Viovy, N., Williams, C., Woodward, F.I., Papale, D., 2010. Terrestrial Gross Carbon Dioxide Uptake: Global Distribution and Covariation with Climate. Science 329, 834–838. https://doi.org/10.1126/science.1184984.

Brown, C.F., Brumby, S.P., Guzder-Williams, B., Birch, T., Hyde, S.B., Mazzariello, J., Czerwinski, W., Pasquarella, V.J., Haertel, R., Ilyushchenko, S., Schwehr, K., Weisse, M., Stolle, F., Hanson, C., Guinan, O., Moore, R., Tait, A.M., 2022. Dynamic World, Near real-time global 10 m land use land cover mapping. Sci Data 9, 251. https://doi.org/10.1038/s41597-022-01307-4.

Bunnell, F.L., Tait, D.E.N., Flanagan, P.W., Van Clever, K., 1977. Microbial respiration and substrate weight loss—I. Soil Biology and Biochemistry 9, 33–40. https://doi.org/10.1016/0038-0717(77)90058-X.

Byrd, R.H., Lu, P., Nocedal, J., Zhu, C., 1995. A Limited Memory Algorithm for Bound Constrained Optimization. SIAM J. Sci. Comput. 16, 1190–1208. https://doi.org/10.1137/0916069.

Chen, M., Griffis, T.J., Baker, J., Wood, J.D., Xiao, K., 2015. Simulating crop phenology in the Community Land Model and its impact on energy and carbon fluxes: Evaluation of CLM crop simulations. J. Geophys. Res. Biogeosci. 120, 310–325. https://doi.org/10.1002/2014JG002780.

Ciais, P., Reichstein, M., Viovy, N., Granier, A., Ogée, J., Allard, V., Aubinet, M., Buchmann, N., Bernhofer, C., Carrara, A., 2005. Europe-wide reduction in primary productivity caused by the heat and drought in 2003. Nature 437, 529–533.

Ciais, P., Wattenbach, M., Vuichard, N., Smith, P., Piao, S.L., Don, A., Luyssaert, S., Janssens, I.A., Bondeau, A., Dechow, R., Leip, A., Smith, P.c., Beer, C., Van Der Werf, G.R., Gervois, S., Van Oost, K., Tomelleri, E., Freibauer, A., Schulze, E.D., Carboeurope synthesis team,, 2010. The European carbon balance. Part 2: croplands. Global Change Biology 16, 1409–1428. https://doi.org/10.1111/j.1365-2486.2009.02055.x.

d'Andrimont, R., Verhegghen, A., Lemoine, G., Kempeneers, P., Meroni, M., van der Velde, M., 2021. From parcel to continental scale – A first European crop type map based on Sentinel-1 and LUCAS Copernicus in-situ observations. Remote Sensing of Environment 266, 112708. https://doi.org/10.1016/j.rse.2021.112708.

Das, N.N., Entekhabi, D., Dunbar, R.S., Chaubell, M.J., Colliander, A., Yueh, S., Jagdhuber, T., Chen, F., Crow, W., O'Neill, P.E., Walker, J.P., Berg, A., Bosch, D.D., Caldwell, T., Cosh, M.H., Collins, C.H., Lopez-Baeza, E., Thibeault, M., 2019. The SMAP and Copernicus Sentinel 1A/B microwave active-passive high resolution surface soil moisture product. Remote Sensing of Environment 233, 111380. https://doi.org/10.1016/j.rse.2019.111380.

Desai, A.R., Richardson, A.D., Moffat, A.M., Kattge, J., Hollinger, D.Y., Barr, A., Falge, E., Noormets, A., Papale, D., Reichstein, M., Stauch, V.J., 2008. Cross-site evaluation of eddy covariance GPP and RE decomposition techniques. Agricultural and Forest Meteorology 148, 821–838. https://doi.org/10.1016/j.agrformet.2007.11.012.

Di Paola, A., Valentini, R., Santini, M., 2016. An overview of available crop growth and yield models for studies and assessments in agriculture: Overview of crop models for agriculture. J. Sci. Food Agric. 96, 709–714. https://doi.org/10.1002/jsfa.7359.

Entekhabi, D., Njoku, E.G., O'Neill, P.E., Kellogg, K.H., Crow, W.T., Edelstein, W.N., Entin, J.K., Goodman, S.D., Jackson, T.J., Johnson, J., Kimball, J., Piepmeier, J.R., Koster, R.D., Martin, N., McDonald, K.C., Moghaddam, M., Moran, S., Reichle, R., Shi, J.C., Spencer, M.W., Thurman, S.W., Tsang, L., Van Zyl, J., 2010. The Soil Moisture Active Passive (SMAP) Mission. Proc. IEEE 98, 704–716. https://doi.org/10.1109/JPROC.2010.2043918.

Farms and farmland in the European Union - statistics [WWW Document], n.d. URL https://ec.europa.eu/eurostat/statistics-explained/index.php?title=Farms_and_farmland_in_the_European_Union_-_statistics (accessed 3.14.23).

I. Fayad P. Ciais M. Schwartz J.-P. Wigneron N. Baghdadi A. de Truchis A. d'Aspremont F. Frappart S. Saatchi A. Pellissier-Tanon H. Bazzi Vision Transformers, a new approach for high-resolution and large-scale mapping of canopy heights 2023 https://doi.org/10.48550/ARXIV.2304.11487.

C. Gerbig F.-T. Koch Biosphere-atmosphere exchange fluxes for CO2 from the Vegetation Photosynthesis and Respiration Model VPRM for 2006–2021 2021 https://doi.org/10.18160/VX78-HVA1.

He, P., Ma, X., Sun, Z., 2022. Interannual variability in summer climate change controls GPP long-term changes. Environmental Research 212, 113409. https://doi.org/10.1016/j.envres.2022.113409.

Hersbach, H., Bell, B., Berrisford, P., Hirahara, S., Horányi, A., Muñoz-Sabater, J., Nicolas, J., Peubey, C., Radu, R., Schepers, D., Simmons, A., Soci, C., Abdalla, S., Abellan, X., Balsamo, G., Bechtold, P., Biavati, G., Bidlot, J., Bonavita, M., Chiara, G., Dahlgren, P., Dee, D., Diamantakis, M., Dragani, R., Flemming, J., Forbes, R., Fuentes, M., Geer, A., Haimberger, L., Healy, S., Hogan, R.J., Hólm, E., Janisková, M., Keeley, S., Laloyaux, P., Lopez, P., Lupu, C., Radnoti, G., Rosnay, P., Rozum, I., Vamborg, F., Villaume, S., Thépaut, J., 2020. The ERA5 global reanalysis. Q.J.R. Meteorol. Soc. 146, 1999–2049. https://doi.org/10.1002/qj.3803.

Hicke, J.A., Lobell, D.B., Asner, G.P., 2004. Cropland Area and Net Primary Production Computed from 30 Years of USDA Agricultural Harvest Data. Earth Interact. 8, 1–20. https://doi.org/10.1175/1087-3562(2004)008<0001:CAANPP>2.0.CO;2.

Hollinger, D.Y., Richardson, A.D., 2005. Uncertainty in eddy covariance measurements and its application to physiological models. Tree Physiology 25, 873–885.

D. Hong B. Zhang X. Li Y. Li C. Li J. Yao N. Yokoya H. Li P. Ghamisi X. Jia A. Plaza G. Paolo J.A. Benediktsson J. Chanussot SpectralGPT: Spectral Foundation Model 2023 https://doi.org/10.48550/ARXIV.2311.07113.

Hong, D., Zhang, B., Li, H., Li, Y., Yao, J., Li, C., Werner, M., Chanussot, J., Zipf, A., Zhu, X.X., 2023. Cross-city matters: A multimodal remote sensing benchmark dataset for cross-city semantic segmentation using high-resolution domain adaptation networks. Remote Sensing of Environment 299, 113856. https://doi.org/10.1016/j.rse.2023.113856.

Howell, T.A., Meek, D.W., Hatfield, J.L., 1983. Relationship of photosynthetically active radiation to shortwave radiation in the San Joaquin Valley. Agricultural Meteorology 28, 157–175. https://doi.org/10.1016/0002-1571(83)90005-5.

Ienco, D., Interdonato, R., Gaetano, R., Minh, D.H.T., 2019. Combining Sentinel-1 and Sentinel-2 Satellite Image Time Series for land cover mapping via a multi-source deep learning architecture. ISPRS Journal of Photogrammetry and Remote Sensing 158, 11–22.

Inglada, J., Vincent, A., Arias, M., Tardy, B., Morin, D., Rodes, I., 2017. Operational High Resolution Land Cover Map Production at the Country Scale Using Satellite Image Time Series. Remote Sensing 9, 95. https://doi.org/10.3390/rs9010095.

Jung, M., Schwalm, C., Migliavacca, M., Walther, S., Camps-Valls, G., Koirala, S., Anthoni, P., Besnard, S., Bodesheim, P., Carvalhais, N., Chevallier, F., Gans, F., Goll, D.S., Haverd, V., Köhler, P., Ichii, K., Jain, A.K., Liu, J., Lombardozzi, D., Nabel, J.E.M.S., Nelson, J.A., O'Sullivan, M., Pallandt, M., Papale, D., Peters, W., Pongratz, J., Rödenbeck, C., Sitch, S., Tramontana, G., Walker, A., Weber, U., Reichstein, M., 2020. Scaling carbon fluxes from eddy covariance sites to globe: synthesis and evaluation of the FLUXCOM approach. Biogeosciences 17, 1343–1365. https://doi.org/10.5194/bg-17-1343-2020.

Keenan, T.F., Prentice, I.C., Canadell, J.G., Williams, C.A., Wang, H., Raupach, M., Collatz, G.J., 2016. Recent pause in the growth rate of atmospheric CO2 due to enhanced terrestrial carbon uptake. Nature Communications 7, 13428.

Kerr, Y.H., Waldteufel, P., Wigneron, J.-P., Martinuzzi, J., Font, J., Berger, M., 2001. Soil moisture retrieval from space: the Soil Moisture and Ocean Salinity (SMOS) mission. IEEE Trans. Geosci. Remote Sensing 39, 1729–1735. https://doi.org/10.1109/36.942551.

Kobayashi, K., Salam, M.U., 2000. Comparing Simulated and Measured Values Using Mean Squared Deviation and its Components. Agron. J. 92, 345. https://doi.org/10.1007/s100870050043.

Kountouris, P., Gerbig, C., Totsche, K.-U., Dolman, A.J., Meesters, A.G.C.A., Broquet, G., Maignan, F., Gioli, B., Montagnani, L., Helfter, C., 2015. An objective prior error quantification for regional atmospheric inverse applications. Biogeosciences 12, 7403–7421. https://doi.org/10.5194/bg-12-7403-2015.

Kountouris, P., Gerbig, C., Rödenbeck, C., Karstens, U., Koch, T.F., Heimann, M., 2018. Technical Note: Atmospheric CO₂ inversions on the mesoscale using data-driven prior uncertainties: methodology and system evaluation. Atmos. Chem. Phys. 18, 3027–3045. https://doi.org/10.5194/acp-18-3027-2018.

Krinner, G., Viovy, N., de Noblet-Ducoudré, N., Ogée, J., Polcher, J., Friedlingstein, P., Ciais, P., Sitch, S., Prentice, I.C., 2005. A dynamic global vegetation model for studies of the coupled atmosphere-biosphere system: DVGM FOR COUPLED CLIMATE STUDIES. Global Biogeochem. Cycles 19. https://doi.org/10.1029/2003GB002199.

Kuppel, S., Peylin, P., Chevallier, F., Bacour, C., Maignan, F., Richardson, A.D., 2012. Constraining a global ecosystem model with multi-site eddy-covariance data. Biogeosciences 9, 3757–3776. https://doi.org/10.5194/bg-9-3757-2012.

Lasslop, G., Reichstein, M., Papale, D., Richardson, A.D., Arneth, A., Barr, A., Stoy, P., Wohlfahrt, G., 2010. Separation of net ecosystem exchange into assimilation and respiration using a light response curve approach: critical issues and global evaluation: SEPARATION OF NEE INTO GPP AND RECO. Global Change Biology 16, 187–208. https://doi.org/10.1111/j.1365-2486.2009.02041.x.

Lawrence, P.J., Chase, T.N., 2007. Representing a new MODIS consistent land surface in the Community Land Model (CLM 3.0). J. Geophys. Res. 112, G01023. https://doi.org/10.1029/2006JG000168.

Lesiv, M., Laso Bayas, J.C., See, L., Duerauer, M., Dahlia, D., Durando, N., Hazarika, R., Kumar Sahariah, P., Vakolyuk, M., Blyshchyk, V., Bilous, A., Perez-Hoyos, A., Gengler, S., Prestele, R., Bilous, S., Akhtar, I., ul H., Singha, K., Choudhury, S.B., Chetri, T., Malek, Ž., Bungnamei, K., Saikia, A., Sahariah, D., Narzary, W., Danylo, O., Sturn, T., Karner, M., McCallum, I., Schepaschenko, D., Moltchanova, E., Fraisl, D., Moorthy, I., Fritz, S., 2019. Estimating the global distribution of field size using crowdsourcing. Glob Change Biol 25, 174–186. https://doi.org/10.1111/gcb.14492.

Levis, S., Bonan, G.B., Kluzek, E., Thornton, P.E., Jones, A., Sacks, W.J., Kucharik, C.J., 2012. Interactive Crop Management in the Community Earth System Model (CESM1): Seasonal Influences on Land-Atmosphere Fluxes. Journal of Climate 25, 4839–4859. https://doi.org/10.1175/JCLI-D-11-00446.1.

Mahadevan, P., Wofsy, S.C., Matross, D.M., Xiao, X., Dunn, A.L., Lin, J.C., Gerbig, C., Munger, J.W., Chow, V.Y., Gottlieb, E.W., 2008. A satellite-based biosphere parameterization for net ecosystem CO 2 exchange: Vegetation Photosynthesis and Respiration Model (VPRM): NET ECOSYSTEM EXCHANGE MODEL. Global Biogeochem. Cycles 22, n/a-n/a. https://doi.org/10.1029/2006GB002735.

Marshall, M., Tu, K., Brown, J., 2018. Optimizing a remote sensing production efficiency model for macro-scale GPP and yield estimation in agroecosystems. Remote Sensing of Environment 217, 258–271. https://doi.org/10.1016/j.rse.2018.08.001.

Migliavacca, M., Reichstein, M., Richardson, A.D., Colombo, R., Sutton, M.A., Lasslop, G., Tomelleri, E., Wohlfahrt, G., Carvalhais, N., Cescatti, A., Mahecha, M.D.,

Montagnani, L., Papale, D., Zaehle, S., Arain, A., Arneth, A., Black, T.A., Carrara, A., Dore, S., Gianelle, D., Helfter, C., Hollinger, D., Kutsch, W.L., Lafleur, P.M., Nouvellon, Y., Rebmann, C., Da, R.O.C.H.A., H.R., Rodeghiero, M., Roupsard, O., Sebastià, M.-T., Seufert, G., Soussana, J.-F., Van Der MOLEN, M.K., 2011. Semiempirical modeling of abiotic and biotic factors controlling ecosystem respiration across eddy covariance sites: SEMIEMPIRICAL MODELING OF ECOSYSTEM RESPIRATION. Global Change Biology 17, 390–409. https://doi.org/10.1111/j.1365-2486.2010.02243.x.

Moffat, A.M., Papale, D., Reichstein, M., Hollinger, D.Y., Richardson, A.D., Barr, A.G., Beckstein, C., Braswell, B.H., Churkina, G., Desai, A.R., Falge, E., Gove, J.H., Heimann, M., Hui, D., Jarvis, A.J., Kattge, J., Noormets, A., Stauch, V.J., 2007. Comprehensive comparison of gap-filling techniques for eddy covariance net carbon fluxes. Agricultural and Forest Meteorology 147, 209–232. https://doi.org/10.1016/j.agrformet.2007.08.011.

Nathaniel, J., Liu, J., Gentine, P., 2023. MetaFlux: Meta-learning global carbon fluxes from sparse spatiotemporal observations. Sci Data 10, 440. https://doi.org/10.1038/s41597-023-02349-y.

Pabon-Moreno, D.E., Migliavacca, M., Reichstein, M., Mahecha, M.D., 2022. On the Potential of Sentinel-2 for Estimating Gross Primary Production. IEEE Trans. Geosci. Remote Sensing 60, 1–12. https://doi.org/10.1109/TGRS.2022.3152272.

Pastorello, G., Trotta, C., Canfora, E., Chu, H., Christianson, D., Cheah, Y.-W., Poindexter, C., Chen, J., Elbashandy, A., Humphrey, M., Isaac, P., Polidori, D., Reichstein, M., Ribeca, A., van Ingen, C., Vuichard, N., Zhang, L., Amiro, B., Ammann, C., Arain, M.A., Ardö, J., Arkebauer, T., Arndt, S.K., Arriga, N., Aubinet, M., Aurela, M., Baldocchi, D., Barr, A., Beamesderfer, E., Marchesini, L.B., Bergeron, O., Beringer, J., Bernhofer, C., Berveiller, D., Billesbach, D., Black, T.A., Blanken, P.D., Bohrer, G., Boike, J., Bolstad, P.V., Bonal, D., Bonnefond, J.-M., Bowling, D.R., Bracho, R., Brodeur, J., Brümmer, C., Buchmann, N., Burban, B., Burns, S.P., Buysse, P., Cale, P., Cavagna, M., Cellier, P., Chen, S., Chini, I., Christensen, T.R., Cleverly, J., Collalti, A., Consalvo, C., Cook, B.D., Cook, D., Coursolle, C., Cremonese, E., Curtis, P.S., D'Andrea, E., da Rocha, H., Dai, X., Davis, K.J., Cinti, B.D., de Grandcourt, A., Ligne, A.D., De Oliveira, R.C., Delpierre, N., Desai, A.R., Di Bella, C.M., di Tommasi, P., Dolman, H., Domingo, F., Dong, G., Dore, S., Duce, P., Dufrêne, E., Dunn, A., Dušek, J., Eamus, D., Eichelmann, U., ElKhidir, H.A.M., Eugster, W., Ewenz, C.M., Ewers, B., Famulari, D., Fares, S., Feigenwinter, I., Feitz, A., Fensholt, R., Filippa, G., Fischer, M., Frank, J., Galvagno, M., Gharun, M., Gianelle, D., Gielen, B., Gioli, B., Gitelson, A., Goded, I., Goeckede, M., Goldstein, A.H., Gough, C.M., Goulden, M.L., Graf, A., Griebel, A., Gruening, C., Grünwald, T., Hammerle, A., Han, S., Han, X., Hansen, B.U., Hanson, C., Hatakka, J., He, Y., Hehn, M., Heinesch, B., Hinko-Najera, N., Hörtnagl, L., Hutley, L., Ibrom, A., Ikawa, H., Jackowicz-Korczynski, M., Janouš, D., Jans, W., Jassal, R., Jiang, S., Kato, T., Khomik, M., Klatt, J., Knohl, A., Knox, S., Kobayashi, H., Koerber, G., Kolle, O., Kosugi, Y., Kotani, A., Kowalski, A., Kruijt, B., Kurbatova, J., Kutsch, W.L., Kwon, H., Launiainen, S., Laurila, T., Law, B., Leuning, R., Li, Y., Liddell, M., Limousin, J.-M., Lion, M., Liska, A.J., Lohila, A., López-Ballesteros, A., López-Blanco, E., Loubet, B., Loustau, D., Lucas-Moffat, A., Lüers, J., Ma, S., Macfarlane, C., Magliulo, V., Maier, R., Mammarella, I., Manca, G., Marcolla, B., Margolis, H.A., Marras, S., Massman, W., Mastepanov, M., Matamala, R., Matthes, J.H., Mazzenga, F., McCaughey, H., McHugh, I., McMillan, A.M.S., Merbold, L., Meyer, W., Meyers, T., Miller, S.D., Minerbi, S., Moderow, U., Monson, R.K., Montagnani, L., Moore, C.E., Moors, E., Moreaux, V., Moureaux, C., Munger, J.W., Nakai, T., Neirynck, J., Nesic, Z., Nicolini, G., Noormets, A., Northwood, M., Nosetto, M., Nouvellon, Y., Novick, K., Oechel, W., Olesen, J.E., Ourcival, J.-M., Papuga, S.A., Parmentier, F.-J., Paul-Limoges, E., Pavelka, M., Peichl, M., Pendall, E., Phillips, R.P., Pilegaard, K., Pirk, N., Posse, G., Powell, T., Prasse, H., Prober, S.M., Rambal, S., Rannik, Ü., Raz-Yaseef, N., Rebmann, C., Reed, D., de Dios, V.R., Restrepo-Coupe, N., Reverter, B.R., Roland, M., Sabbatini, S., Sachs, T., Saleska, S.R., Sánchez-Cañete, E.P., Sanchez-Mejia, Z.M., Schmid, H.P., Schmidt, M., Schneider, K., Schrader, F., Schroder, I., Scott, R.L., Sedlák, P., Serrano-Ortíz, P., Shao, C., Shi, P., Shironya, I., Siebicke, L., Šigut, L., Silberstein, R., Sirca, C., Spano, D., Steinbrecher, R., Stevens, R.M., Sturtevant, C., Suyker, A., Tagesson, T., Takanashi, S., Tang, Y., Tapper, N., Thom, J., Tomassucci, M., Tuovinen, J.-P., Urbanski, S., Valentini, R., van der Molen, M., van Gorsel, E., van Huissteden, K., Varlagin, A., Verfaillie, J., Vesala, T., Vincke, C., Vitale, D., Vygodskaya, N., Walker, J.P., Walter-Shea, E., Wang, H., Weber, R., Westermann, S., Wille, C., Wofsy, S., Wohlfahrt, G., Wolf, S., Woodgate, W., Li, Y., Zampedri, R., Zhang, J., Zhou, G., Zona, D., Agarwal, D., Biraud, S., Torn, M., Papale, D., 2020. The FLUXNET2015 dataset and the ONEFlux processing pipeline for eddy covariance data. Sci Data 7, 225. https://doi.org/10.1038/s41597-020-0534-3.

Pique, G., Fieuzal, R., Al Bitar, A., Veloso, A., Tallec, T., Brut, A., Ferlicoq, M., Zawilski, B., Dejoux, J.-F., Gibrin, H., Ceschia, E., 2020. Estimation of daily CO2 fluxes and of the components of the carbon budget for winter wheat by the assimilation of Sentinel 2-like remote sensing data into a crop model. Geoderma 376, 114428. https://doi.org/10.1016/j.geoderma.2020.114428.

Potapov, P., Turubanova, S., Hansen, M.C., Tyukavina, A., Zalles, V., Khan, A., Song, X.-P., Pickens, A., Shen, Q., Cortez, J., 2021. Global maps of cropland extent and change show accelerated cropland expansion in the twenty-first century. Nat Food 3, 19–28. https://doi.org/10.1038/s43016-021-00429-z.

Potter, C.S., Randerson, J.T., Field, C.B., Matson, P.A., Vitousek, P.M., Mooney, H.A., Klooster, S.A., 1993. Terrestrial ecosystem production: A process model based on global satellite and surface data. Global Biogeochem. Cycles 7, 811–841. https://doi.org/10.1029/93GB02725.

Reeves, M.C., Zhao, M., Running, S.W., 2005. Usefulness and limits of MODIS GPP for estimating wheat yield. International Journal of Remote Sensing 26, 1403–1421. https://doi.org/10.1080/01431160512331326567.

Reichstein, M., 2003. Inverse modeling of seasonal drought effects on canopy CO_2/H_2O exchange in three Mediterranean ecosystems. J. Geophys. Res. 108, 4726. https://doi.org/10.1029/2003JD003430.

Reichstein, M., Tenhunen, J.D., Roupsard, O., Ourcival, J.-M., Rambal, S., Dore, S., Valentini, R., 2002. Ecosystem respiration in two Mediterranean evergreen Holm Oak forests: drought effects and decomposition dynamics: *Analysis of ecosystem respiration*. Functional Ecology 16, 27–39. https://doi.org/10.1046/j.0269-8463.2001.00597.x.

Reichstein, M., Bahn, M., Ciais, P., Frank, D., Mahecha, M.D., Seneviratne, S.I., Zscheischler, J., Beer, C., Buchmann, N., Frank, D.C., 2013. Climate extremes and the carbon cycle. Nature 500, 287–295.

Revill, A., Sus, O., Barrett, B., Williams, M., 2013. Carbon cycling of European croplands: A framework for the assimilation of optical and microwave Earth observation data. Remote Sensing of Environment 137, 84–93. https://doi.org/10.1016/j.rse.2013.06.002.

Roy, D.P., Li, J., Zhang, H.K., Yan, L., Huang, H., Li, Z., 2017. Examination of Sentinel-2A multi-spectral instrument (MSI) reflectance anisotropy and the suitability of a general method to normalize MSI reflectance to nadir BRDF adjusted reflectance. Remote Sensing of Environment 199, 25–38. https://doi.org/10.1016/j.rse.2017.06.019.

Santaren, D., Peylin, P., Viovy, N., Ciais, P., 2007. Optimizing a process-based ecosystem model with eddy-covariance flux measurements: A pine forest in southern France: MODEL OPTIMIZATION USING FLUX DATA. Global Biogeochem. Cycles 21, n/a-n/a. https://doi.org/10.1029/2006GB002834.

Santaren, D., Peylin, P., Bacour, C., Ciais, P., Longdoz, B., 2014. Ecosystem model optimization using in situ flux observations: benefit of Monte Carlo versus variational schemes and analyses of the year-to-year model performances. Biogeosciences 11, 7137–7158. https://doi.org/10.5194/bg-11-7137-2014.

Schaefer, K., Schwalm, C.R., Williams, C., Arain, M.A., Barr, A., Chen, J.M., Davis, K.J., Dimitrov, D., Hilton, T.W., Hollinger, D.Y., Humphreys, E., Poulter, B., Raczka, B.M., Richardson, A.D., Sahoo, A., Thornton, P., Vargas, R., Verbeeck, H., Anderson, R., Baker, I., Black, T.A., Bolstad, P., Chen, J., Curtis, P.S., Desai, A.R., Dietze, M., Dragoni, D., Gough, C., Grant, R.F., Gu, L., Jain, A., Kucharik, C., Law, B., Liu, S., Lokipitiya, E., Margolis, H.A., Matamala, R., McCaughey, J.H., Monson, R., Munger, J.W., Oechel, W., Peng, C., Price, D.T., Ricciuto, D., Riley, W.J., Roulet, N., Tian, H., Tonitto, C., Torn, M., Weng, E., Zhou, X., 2012. A model-data comparison of gross primary productivity: Results from the North American Carbon Program site synthesis: A MODEL-DATA COMPARISON OF GPP. J. Geophys. Res. 117, n/a-n/a. https://doi.org/10.1029/2012JG001960.

Sellers, P.J., Mintz, Y., Sud, Y.C., Dalcher, A., 1986. A Simple Biosphere Model (SIB) for Use within General Circulation Models. J. Atmos. Sci. 43, 505–531. https://doi.org/10.1175/1520-0469(1986)043<0505:ASBMFU>2.0.CO;2.

Smith, B., Prentice, I.C., Sykes, M.T., 2001. Representation of vegetation dynamics in the modelling of terrestrial ecosystems: comparing two contrasting approaches within European climate space: *Vegetation dynamics in ecosystem models*. Global Ecology and Biogeography 10, 621–637. https://doi.org/10.1046/j.1466-822X.2001.t01-1-00256.x.

Smith, B., Wårlind, D., Arneth, A., Hickler, T., Leadley, P., Siltberg, J., Zaehle, S., 2014. Implications of incorporating N cycling and N limitations on primary production in an individual-based dynamic vegetation model. Biogeosciences 11, 2027–2054. https://doi.org/10.5194/bg-11-2027-2014.

Tarantola, A., 1987. Inverse problem theory: methods for data fitting and model parameter estimation. Elsevier ; Distributors for the United States and Canada, Elsevier Science Pub. Co, Amsterdam ; New York : New York, NY, U.S.A.

Taylor, K.E., 2001. Summarizing multiple aspects of model performance in a single diagram. Journal of Geophysical Research: Atmospheres 106, 7183–7192.

Xiao, X., 2004. Modeling gross primary production of temperate deciduous broadleaf forest using satellite images and climate data. Remote Sensing of Environment 91, 256–270. https://doi.org/10.1016/j.rse.2004.03.010.

Xiao, X., Hollinger, D., Aber, J., Goltz, M., Davidson, E.A., Zhang, Q., Moore, B., 2004. Satellite-based modeling of gross primary production in an evergreen needleleaf forest. Remote Sensing of Environment 89, 519–534. https://doi.org/10.1016/j.rse.2003.11.008.

Zeng, N., Zhao, F., Collatz, G.J., Kalnay, E., Salawitch, R.J., West, T.O., Guanter, L., 2014. Agricultural Green Revolution as a driver of increasing atmospheric CO2 seasonal amplitude. Nature 515, 394–397. https://doi.org/10.1038/nature13893.

Zhang, Y., Bastos, A., Maignan, F., Goll, D., Boucher, O., Li, L., Cescatti, A., Vuichard, N., Chen, X., Ammann, C., Arain, M.A., Black, T.A., Chojnicki, B., Kato, T., Mammarella, I., Montagnani, L., Roupsard, O., Sanz, M.J., Siebicke, L., Urbaniak, M., Vaccari, F.P., Wohlfahrt, G., Woodgate, W., Ciais, P., 2020. Modeling the impacts of diffuse light fraction on photosynthesis in ORCHIDEE (v5453) land surface model. Geosci. Model Dev. 13, 5401–5423. https://doi.org/10.5194/gmd-13-5401-2020.